The ESCRT-III Protein CHMP1A Mediates Secretion of Sonic Hedgehog on a Distinctive Subtype of Extracellular Vesicles

Michael Coulter, Cristina Dorobantu, Gerrald Lodewijk, Francois Delalande, Sarah Cianférani, Vijay Ganesh, Richard Smith, Elaine Lim, C. Shan Xu, Song Pang, et al.

The ESCRT-III protein CHMP1A mediates secretion of sonic hedgehog on a novel class of extracellular vesicles

Michael E. Coulter[1,2‡], Cristina M. Dorobantu[3‡], Gerrald A. Lodewijk[4‡], François Delalande[5], Sarah Cianferani[5], Vijay Ganesh[1,6], Richard Smith[1], Elaine T. Lim[1], C. Shan Xu[7], Song Pang[7], Eric T. Wong[8], Hart G.W. Lidov[9], Monica L. Calicchio[9], Edward Yang[10], Dilenny M. Gonzalez[1], Thorsten Schlaeger[11], Ganesh Mochida[1,12], Harald Hess[7], Wei-Chung Allen Lee[13], Maria K. Lehtinen[9], Tomas Kirchhausen[14], David Haussler[15], Frank M.J. Jacobs[4*], Raphael Gaudin[3,14*], Christopher A. Walsh[1*]

1. Division of Genetics and Genomics and Howard Hughes Medical Institute, Boston Children's Hospital, Departments of Pediatrics and Neurology, Harvard Medical School, Boston, MA 02115, USA
2. Program in Neuroscience and Harvard/MIT MD-PHD Program, Harvard Medical School, Boston, MA 02115, USA
3. Inserm U1110, Université de Strasbourg, Institut de Recherche sur les Maladies Virales et Hépatiques, CS90032 Strasbourg, France
4. Faculty of Science, Swammerdam Institute for Life Sciences, University of Amsterdam, 1000 GG Amsterdam, The Netherlands
5. Laboratoire de Spectrométrie de Masse Bio-Organique, IPHC, UMR 7178, CNRS-Université de Strasbourg, ECPM, CS90032 Strasbourg, France
6. Department of Neurology, Massachusetts General Hospital, Boston, MA 02114 and Department of Neurology, Brigham and Women's Hospital, Boston, MA 02115, USA
7. Janelia Research Campus, Howard Hughes Medical Institute, Ashburn, VA 20147, USA
8. Brain Tumor Center and Neuro-Oncology Unit, Beth Israel Deaconess Medical Center, Boston, MA 02115, USA
9. Department of Pathology, Boston Children's Hospital, Boston, MA 02115, USA
10. Department of Radiology, Boston Children's Hospital, Boston, MA 02115, USA
11. Division of Hematology and Oncology, Boston Children's Hospital, Boston, MA 02115, USA
12. Pediatric Neurology Unit, Department of Neurology, Massachusetts General Hospital, Boston, MA 02114, USA
13. F.M. Kirby Neurobiology Center, Boston Children's Hospital and Department of Neurology, Harvard Medical School, Boston, MA 02115, USA
14. Program in Cellular and Molecular Medicine, Boston Children's Hospital and Departments of Pediatrics and Cell Biology, Harvard Medical School, Boston, MA 02115, USA
15. Center for Biomolecular Science and Engineering, University of California and Howard Hughes Medical Institute, Santa Cruz, CA 95064, USA

‡ These authors contributed equally to this work

***Corresponding Authors:**

Christopher A. Walsh

Division of Genetics and Genomics

Children's Hospital Boston

3 Blackfan Circle, CLS 15049

Boston, MA 02115 USA

Email: christopher.walsh@childrens.harvard.edu

Raphael Gaudin

Inserm U1110

Université de Strasbourg

Institut de Recherche sur les Maladies Virales et Hépatiques

CS90032 Strasbourg, France

Email: rgaudin@unistra.fr

Frank Jacobs

Faculty of Science

Swammerdam Institute for Life Sciences, University of Amsterdam

1000 GG Amsterdam, The Netherlands

Email: F.M.J.Jacobs@uva.nl

SUMMARY (150 max)

Endosomal Sorting Complex Required for Transport (ESCRT) complex proteins regulate biogenesis and release of extracellular vesicles (EVs), which enable cell-to-cell communication in the nervous system that is essential for development and adult function. We recently showed human loss of function (LOF) mutations in the ESCRT-III member *CHMP1A* cause autosomal recessive microcephaly with pontocerebellar hypoplasia (Mochida et al., 2012). Here, we show *Chmp1a* is required for progenitor proliferation in mouse cortex and cerebellum, and progenitor maintenance in human cerebral organoids. *CHMP1A* regulates proliferation through Sonic hedgehog (SHH) secretion. Loss of *CHMP1A* reduces intraluminal vesicle (ILV) formation in multivesicular bodies (MVBs) and EV release, and SHH protein is present on ART-EVs, a new EV subtype marked by a unique set of proteins. *CHMP1A* loss specifically impairs secretion of SHH on ART-EVs. *CHMP1A*'s requirement in the formation of ART-EVs and other EVs provides a model to elucidate EV functions in multiple brain processes.

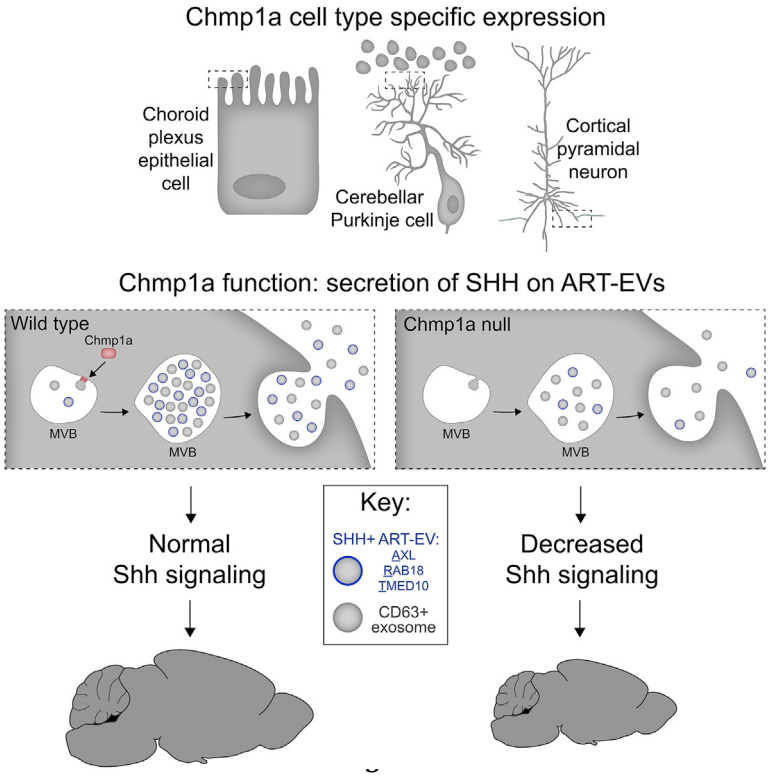

INTRODUCTION

EVs are increasingly recognized as essential mediators of specialized cellular secretion, but the mechanisms of EV function are not well understood, in part because of the diversity of EV classes (Bobrie et al., 2012, Kowal et al., 2016) and the lack of tools to specifically disrupt individual EV classes. EVs are essential for cell-to-cell communication by allowing hydrophobic signaling molecules (Korkut et al., 2009), RNA (Tietje et al., 2014), and other specialized cargo (Budnik et al., 2016) to travel through an aqueous extracellular environment. At *Drosophila* neuromuscular junction, EV-mediated wingless secretion is required for synapse growth, and EV-mediated Synaptotagmin 4 secretion is required for retrograde signaling (Koles et al., 2012; Korkut et al., 2009; Korkut et al., 2013). Cultured mammalian neurons (Lachenal et al., 2011), oligodendrocytes (Fruhbeis et al., 2013), and microglia (Antonucci et al., 2012) secrete EVs that have been proposed to modulate synaptic strength and cell viability analogously, and perhaps even to mediate pathological transfer of RNAs, prion-like proteins, and Tau proteins (Asai et al., 2015). However, these functions remains somewhat speculative because of a lack of *in vivo* vertebrate models that selectively disrupt EV function.

Shh is a hydrophobic secreted factor essential for embryonic development, serving as a morphogen (Cohen et al., 2015; Roelink et al., 1995), a mitogen (Nielsen and Dymecki, 2010; Dahmane and Ruiz i Altaba, 1999), an axon guidance molecule (Wilson and Stoeckli, 2013; Charron et al., 2003), and a regulator of synapse formation (Harwell et al., 2012). In developing cerebellum, Shh stimulates proliferation of precursors that generate granule neurons (GCPs), the most abundant neuron in brain (Zhou et al., 2007), and loss of *Shh* causes profound cerebellar hypoplasia (Corrales et al., 2006). Whereas the source of secreted Shh that regulates GCP proliferation is Purkinje cells (PC) (Wechsler-Reya and Scott, 1999), the mechanism of Shh

secretion is unclear because studies have reported multiple different secretion mechanisms including oligomeric complexes (Zeng et al., 2001), lipoprotein particles (Panakova et al., 2005), and exovesicles (Matusek et al., 2014), including exosomes (Vyas et al., 2014).

ESCRT machinery regulates EV formation and release as well as other membrane remodeling processes in the cell. ESCRT members are grouped into four subunits (0 to III) that drive different steps in membrane remodeling including deformation, budding, and scission (McCullough et al., 2013). The ESCRT-III complex comprises eleven subunits designated CHMPs (Charged Multivesicular Body Proteins) particularly important for membrane scission. Several conflicting potential mechanisms have been proposed to explain why LOF mutations in an ESCRT-III member, *CHMP1A*, cause microcephaly with pontocerebellar hypoplasia and short stature in humans (Mochida et al., 2012, Howard et al., 2001). Here, we show that, analogous to *Drosophila* (Matusek et al., 2014), *CHMP1A* is an essential mediator of vertebrate SHH secretion during brain development. *Chmp1a* null mice show widespread defects in forebrain and hindbrain development with evidence of disrupted *Shh* signaling, which can be rescued by activation of downstream signaling. Further, Shh protein level in the cerebrospinal fluid (CSF) of *Chmp1a* null embryos is markedly reduced compared to littermate controls. *Chmp1a* is specifically required for vesicular SHH secretion. *Chmp1a* loss impairs EV biogenesis by reducing ILVs within MVBs and disrupts secretion of a unique SHH-positive EV subtype we call ART-EVs as well as exosomes. *CHMP1A* function reveals an unexpected diversity and specificity of EV subtypes, and provides an essential vertebrate model to dissect EV function.

RESULTS

Chmp1a is required for embryonic development

We created a *Chmp1a* gene trap (GT) mouse line as shown in **Figure S1** that completely removes Chmp1a protein. A gene trap cassette (Stryke et al., 2003) inserted in intron 1 of *Chmp1a* contains a strong splice acceptor from *En2* fused to the coding sequence for beta-galactosidase (**Figure S1A**). ES cells containing this GT allele were injected into mouse blastocysts to generate *Chmp1a* GT chimeras, which were outcrossed to create germline *Chmp1a* GT allele carriers. DNA sequencing confirms that in homozygous GT embryos, *Chmp1a* intron 1 is fused to *En* intron 1 (**Figure S1C**). Heterozygous GT mice show reduced Chmp1a protein expression compared to wild type (WT) and homozygous GT mice express no detectable Chmp1a protein (**Figure S1B**), confirming a null mutation.

Chmp1a is required for normal embryonic development and postnatal survival in mice, with *Chmp1a* null embryos being significantly smaller than littermate controls during embryogenesis and 40% smaller than controls at birth (two-tailed t-test, $p = 2x10^{-5}$; **Figures 1A, 1C**). *Chmp1a* null mice die at or soon after birth (**Figure S1D**), with brains that are 14% smaller than controls (two-tailed t-test, p = 0.01, **Figures 1B, 1D**), while *Chmp1a* heterozygous mice are indistinguishable from wild type controls, and hence are combined with WT in all analyses (**Figures S1E, S1F**). *Chmp1a* null mice have smaller olfactory bulbs, a smaller and thinner cerebral cortex, smaller striatum, and a smaller cerebellum with reduced foliation (**Figures 1E-H, S1G**). Together, reduced body size, microcephaly, reduced basal ganglia, and cerebellar hypoplasia in *Chmp1a* null mice closely models the phenotype of *CHMP1A* null patients (Mochida et al., 2012; **Figure S2**).

Chmp1a is expressed in post-mitotic neurons and choroid plexus during brain development

Insertion of lacZ into the *Chmp1a* locus provided crucial information about normal expression that suggested potential mechanisms. Heterozygous GT mice show expression of *Chmp1a-lacZ* in developing cerebellum and hindbrain choroid plexus (ChP) (**Figures 2A, S3C**). At postnatal day (P) 4, the peak of GCP proliferation, *Chmp1a-lacZ* is specifically expressed in PC layer (**Figure 2A**) and is undetectable in GCPs. Immunofluorescence confirmed the localization of Chmp1a protein in ChP and in PCs in the developing cerebellum with little expression in GCPs of the external granule layer (EGL) (**Figures 2B, S3D**). RNAscope in developing human cerebellum (gestational week (GW) 20) confirmed *CHMP1A* expression in the PC layer, identified as the cell layer expressing *SHH* and superficial to *PTCH* positive internal granule layer (**Figure 2C**), and further showed that *SHH*, *CHMP1A*, and CD63 are expressed in the same cell population, suggesting co-expression in PCs (**Figure 2D**). Immunostaining showed Chmp1a expression in AQP1-positive choroid plexus epithelial cells (**Figure S3A**), confirming RNA-sequencing from purified epithelial cells (Lun et al., 2015a). In developing mouse cerebral cortex, Chmp1a immunoreactivity is enriched in post-mitotic neurons of the cortical plate compared to ventricular zone progenitors (**Figure 2E**), and RNAscope in developing human cortex (GW20) confirmed *CHMP1A* expression in the cortical plate along with *CD63*, whereas the downstream *SHH* target *PTCH* is expressed in a complementary fashion in dividing progenitors of the ventricular zone (**Figures 2F, S3B**). The similar expression patterns of *SHH, CD63*, and *CHMP1A* in postmitotic neurons, with the complementary expression of *PTCH* in progenitors, suggest non cell-autonomous roles for *CHMP1A* in proliferation via regulation of one or more secreted factors, such as SHH.

Chmp1a is essential for neuroprogenitor proliferation

Chmp1a null mouse embryos show defects in progenitor proliferation in cerebellum, cortex, and basal ganglia (**Figure 3**). At P0, the latest age we can study due to lethality, GCP proliferation in the developing cerebellum is significantly impaired in *Chmp1a* null mice with 40% fewer mitotic GCPs than littermate controls (labeled with phosphorylated histone H3 (pH3), two-tailed t-test, p = 0.0001; **Figure 3A**). This deficit is twice as large as the reduction in mitotic progenitors in the developing cortex and matches human *CHMP1A* null patients, whose cerebellar hypoplasia is strikingly severe in relation to more modest microcephaly (Mochida et al., 2012; **Figure S2**). The overall size of the cerebellum is already reduced at P0 in *Chmp1a* null mice (**Figure 1G**), with a 20% reduction in mitotic GCP density compared to controls (two-tailed t-test, p = 0.0009; **Figure 3A**), whereas PCs are not detectably affected in mutant mice (cerebellum area: 36% vs 33%, two-tailed t-test, p = 0.16; **Figures S4A, S4B**),

Chmp1a null embryos have decreased anterior to posterior cerebral cortex length (**Figure 1B**), a 13% thinner cortex (two-tailed t-test, p = 0.03), and defects in cortical layers (**Figure 1E**); all suggesting defects in cortical neurogenesis. Superficial cortical layers (II-IV, Cux1 positive neurons) are reduced by 25% in the mutants (two-tailed t-test, p = 0.002), while deep cortical layers (V-VI, Ctip2 positive neurons) are less affected (9% reduction, two-tailed t-test, p = 0.08; **Figure 1E**). Preferential reduction of upper cortical layers commonly reflects defects of cortical neurogenesis (Lizarraga et al., 2010), since cortical layers form in an inside-out sequence, with deep-layer neurons born first and upper-layer neurons born last (Greig et al., 2013). Quantification of mitotic ventricular zone progenitors at embryonic day (E) 14.5 showed 20% fewer mitotic ventricular zone progenitors in mutants compared to controls (two-tailed t-test, p = 0.003; **Figure 3B**) and, at E13.5, mutant embryos had 26% fewer Tbr2 positive intermediate

progenitors than controls (two-tailed t-test, p = 0.035, **Figure 3C**). *Chmp1a* null embryos had no detectable increase in cleaved caspase-3 positive apoptotic cells (**Figures S4C, S4D**) and intact epithelial structure with normal localization of key proteins such as aPKC and beta-catenin (**Figure S4E**), suggesting that the microcephaly and cortical thinning result from decreased progenitor proliferation. Mutant embryos also showed normal progression of cytokinesis in cortical progenitors measured by the ratio of pH3-positive early mitotic cells to aurora A-positive cells undergoing abscission (**Figures S5A, B**) and normal DNA content measured by Propidium iodide staining of embryonic fibroblasts (MEFs) (**Figure S5D**). These data suggest loss of *Chmp1a* causes defects in proliferation, but not cytokinesis, a process in which the ESCRT complex has also been implicated (Carlton et al., 2012).

In late-embryonic ventral telencephalon, the striatum is 25% smaller in the absence of *Chmp1a* (two-tailed t-test, p = 0.0004; **Figure 1F**), which results from decreased progenitor proliferation at E12.5 in MGE and LGE. Immunostaining for pH3 during MGE and LGE neurogenesis (E12.5) shows a dramatic 43% reduction in pH3 positive progenitors in *Chmp1a* null embryos (two-tailed t-test, p = 0.016; **Figure 3D**), revealing essential roles for *Chmp1a* in ventral telencephalon that are also seen in humans with *CHMP1A* mutations (**Figure S2**).

Chmp1a is essential for Shh-mediated progenitor proliferation

Since Shh is the primary mitogen that drives GCP proliferation (Corrales et al., 2004; Dahmane and Ruiz i Altaba, 1999), the reduced GCP proliferation in *Chmp1a* null mice prompted examination of whether *Chmp1a* is required for Shh-mediated proliferation. In control mice at birth, *Shh* signaling is more active anteriorly than dorsally in the cerebellum (Corrales et al., 2004), with almost twice the number of mitotic GCPs (pH3+) in anterior EGL compared to

dorsal EGL. In *Chmp1a* null mice, this difference was substantially reduced to 1.25-fold (two-tailed t-test, p = 0.005; **Figures S4F, S4G**) consistent with defective *Shh* signaling. *In situ* hybridization for *Ptch*, a downstream target of *Shh* signaling, revealed lower *Ptch* expression in *Chmp1a* null cerebellum that was especially pronounced in the Shh-responsive EGL (**Figure 3E**), providing further evidence for decreased *Shh* signaling in the absence of *Chmp1a*.

Chmp1a is required for Shh secretion *in vivo*

Direct measurement of total Shh protein concentration with a highly sensitive ELISA assay showed 40% less Shh in embryonic CSF from *Chmp1a* null mouse embryos compared to controls at E14.5 (two-tailed t-test, p = 0.009; **Figure 3F**), providing direct evidence that *Chmp1a* is required for Shh secretion in the developing brain. In parallel, SAG stimulation of *Chmp1a* null and control MEFs showed no significant defect in downstream *Shh* signaling as measured by *Gli1* activation (two-tailed t-test, p = 0.39; **Figure S6B**), consistent with *Chmp1a* acting upstream of *Shh*. Furthermore, we performed a rescue experiment with a *Ptch* heterozygous null mouse, a genetic tool that increases *Shh* signaling *in vivo* (Goodrich et al., 1997), and found that *Chmp1a* null embryo microcephaly at E18.5 was reversed in *Chmp1a* null : *Ptch* heterozygous embryos and not significantly different from control (two-tailed t-test, p = 0.22, **Figure S6A**). This result provides further evidence that microcephaly in *Chmp1a* null mice reflects decreased Shh function.

CHMP1A is essential for human cerebral organoid formation

To further examine *CHMP1A's* role in SHH-driven neuroprogenitor proliferation, we generated *CHMP1A* null human cerebral organoids using CRISPR/Cas9 mutagenesis and found

impaired progenitor maintenance and premature neuronal differentiation (**Figures 4, S7A**). Immunostaining of day 38 organoids for PAX6 and CTIP2 showed a 67% loss of PAX6-positive progenitor cell area and 123% gain of CTIP2-positive postmitotic neurons (two-tailed t-test, CTIP2: $p = 0.001$, PAX6: $p = 0.003$, **Figures 4B, 4C**). RNA sequencing of iPSCs before differentiation, organoids at day 14 during differentiation, and organoids at day 38 after differentiation (**Figure S7B, S7C**) further defined the defect in organoid formation as impaired progenitor maintenance and premature neuronal differentiation. GO pathway analysis of upregulated genes in *CHMP1A* null organoids showed enrichment of terms for neuronal differentiation (**Figure 4D**). RNA sequencing revealed distinct groups of up- and down-regulated genes in the absence of *CHMP1A* including loss of progenitor markers (*SOX1, SOX2, HMGA1*, and *HES5*) and early induction of differentiated neuron markers (*DCX*, *SYT4*, *ROBO2*, and *NRXN1*) (DESeq2 adjusted p-value, each gene: $p < 0.05$, **Figures 4E, 4F, Tables S1, S2**). *CHMP1A* null day 38 organoids correlate more closely with RNAseq data from GW12 human cortex (Allen Institute), while control organoids correlate more closely with GW9 cortex, providing additional evidence for premature differentiation (**Figure 4G**). At day 38, *CHMP1A* null organoids show decreased expression of progenitor marker *PAX6* and increased expression of post-mitotic neuron marker *CTIP2* (**Figures 4H**).

RNA sequencing revealed impaired *SHH* signaling with 50% reduction of *GLI1* expression in mutant iPSCs at the start of organoid differentiation (DESeq2 adjusted p-value, iPSC: $p < 0.0001$, **Figure 4I**). Activation of *SHH* signaling with exogenous administration of SAG on differentiation day 35 (with harvest on day 38, **Figure 4A**) induced *GLI1* and *PTCH* expression equally in WT and *CHMP1A* null organoids (two-tailed t-test, *GLI1*: $p = 0.75$, *PTCH*: $p = 0.84$), suggesting no downstream *SHH* signaling defect in the absence of *CHMP1A* (**Figure**

4J). Rather, SAG-induced *SHH* signaling rescued reduced expression of *PAX6* in *CHMP1A* null organoids, a defining marker of impaired progenitor maintenance in the absence of *CHMP1A* (DESeq2 adjusted p-value, no treatment: $p < 0.0001$, +SAG: $p = 0.11$, **Figure 4K)**, although some gene expression differences were not rescued (**Figure S8**). These data strongly suggest that progenitor proliferation defects in the absence of *CHMP1A* result from upstream impairment of *SHH* signaling via decreased SHH secretion.

Defective ILV and MVB structure in *Chmp1a* null embryos

As Shh secretion has been reported on EVs and ESCRT-III is involved in ILV biogenesis in MVBs, we used three-dimensional focused ion bean scanning electron microscopy (FIB-SEM, Xu et al., 2017) to examine choroid plexus (ChP) epithelial cells, a primary source of Shh in embryonic mouse brain (Nielsen and Dymecki, 2010; Lun et al., 2015a), and found abundant MVBs near the ventricular surface (**Figure 5**). SEM revealed the ChP's remarkable structure as a monolayer of epithelial cells forming grape-like clusters that maximize ventricular surface area (**Figure 5A**) and transmission EM (TEM) showed the ventricular surface cross-section (**Figure 5B**). FIB-SEM imaging revealed that 75% of MVBs in ChP epithelial cells were located within 2 µm of the ventricular surface, indicating some could be secretory MVBs (**Figures 5C, 5D**). Indeed, one MVB showed fusion with the ventricular surface (**Figure 5E**). CHMP1A immunoreactivity in human hindbrain ChP epithelial cells distributed together with CD63-immunoreactive MVBs near the ventricular surface (**Figure S9A**) providing additional evidence of secretory MVBs. MVB fusion with the plasma membrane releases ILVs as EVs and exosomes (Tietje et al., 2014). Thus, our imaging provides evidence that ChP epithelial cells are a source of EVs in the developing brain.

TEM showed disrupted MVB structure in *Chmp1a* null embryonic ChP. The number of ILVs per MVB was 33% lower in mutant ChP epithelial cells than in control (Mann-Whitney test, p = 0.0003; **Figures 5F, 5G, S9C**), and some *Chmp1a* null MVBs contained abnormally large ILVs (**Figure 5F**, arrowhead), a known consequence of impaired ILV budding (Lee et al., 2007). Apart from the observed defects in EV biogenesis, the ChP ventricular surface and microvilli appeared otherwise normal in *Chmp1a* null embryos (**Figures S9B**). As in ChP epithelial cells, P0 mutant cerebellar PC MVBs showed 22% fewer ILVs per MVB compared to controls (Mann-Whitney test, p = 0.0005; **Figures 5H, 5I, S9D**). These data raise the possibility that defective Shh secretion into the CSF and from PCs may involve defective ILV formation in the MVB. TEM showed MVBs are abundant in dendrites of both PC and cortical projection neurons. At P4, cerebellar PC MVBs are common in the dendrites that extend towards the EGL where Shh-responsive GCPs are located (**Figures S10A, S10B**). In mouse cerebral cortex, serial reconstruction of hundreds of TEM images of cortical pyramidal neurons (Lee et al., 2016) shows that MVBs are surprisingly abundant in pyramidal cell dendrites (**Figure S10C**). The dendritic arbor and axon of a single pyramidal cell contained at least 80 MVBs, often near synapses, which could be interpreted as active dendritic EV secretion sites. Indeed, Shh released from pyramidal cell dendrites during postnatal development is required for synapse formation between layer V corticofugal projection neurons and callosal projection neurons in the cortex (Harwell et al., 2012). These finding suggest EV-mediated secretion is widespread across multiple time points and anatomic regions of the developing brain.

CHMP1A is required for vesicular SHH secretion *in vitro*

To dissect the mechanism underlying regulation of SHH secretion by *CHMP1A*, we used the human fetal glial cell line SVG-A and generated *CHMP1A* null monoclonal lines through CRISPR/Cas9 mutagenesis (**Figures S11A, S11B**). TEM of mutant cells showed a 32% reduction of ILVs per MVB in *CHMP1A* null compared to WT (Mann-Whitney test, $p = 0.0012$; **Figures 6A, 6B**), confirming our *in vivo* results from choroid plexus and Purkinje cells (**Figure 5**). Serial ultracentrifugation of conditioned medium obtained from *SHH*-expressing SVG-A cells enabled EV collection and initial separation based on size (Kowal et al, 2016, Methods, and **Figure 6C**): large EVs and cell debris pelleted in the 2K fraction, medium-sized EVs in the 10K fraction, and small EVs and exosomes in in the 100K fraction. The exosome-specific markers CD9, CD81, CD63, TSG101 and Syntenin were either restricted to or highly enriched in the 100K pellet, while exosome-excluded markers, such as actin and ER-resident protein GP96 were absent from this fraction (**Figure 6D**), confirming previous reports (Lotvall et al., 2014). In the *CHMP1A* null 100K pellet, CD63 was decreased 46% and Syntenin was decreased 55% (two-tailed t-test, CD63: $p = 0.001$, Syntenin: $p = 0.037$), while CD9, CD81, and TSG101 were not detectably changed (two-tailed t-test, CD9: $p = 0.42$, CD81: $p = 0.75$, TSG101: $p = 0.61$, **Figure 6E**). Although SHH was detected in all vesicular fractions, it was significantly decreased only in the 100K EV fraction derived from *CHMP1A* null SVG-A cells (49% reduction, two-tailed t-test, $p = 0.003$, **Figure 6F**). Similar results were obtained using a heterogeneous pool of *CHMP1A* null cells (**Figure S11C**) instead of a monoclonal population. Importantly, the 100K fraction contained biologically active SHH that induced *Gli1* expression in NIH3T3 cells. At equal protein content, the signaling potency of the 100K EV fraction was reduced 79% in *CHMP1A*

null cells compared to EVs of WT cells (6ug protein, two-tailed t-test, p = 0.008, **Figure 6G**), demonstrating that *CHMP1A* is required for secretion of active SHH-containing small EVs.

SHH is secreted on specialized EVs

Because the 100K pellet formed following ultracentrifugation is a complex mixture of several distinct EVs subtypes, we next used immunoisolation to determine which subtype contained SHH-positive vesicles (Kowal et al., 2016, Figure 7A). We immunoisolated with anti-CD9 or anti-CD63 antibodies to test for the presence of SHH on exosomes. Western Blot (WB) analysis of bound and unbound material showed modest SHH amounts on CD9-positive EVs and minimal SHH on CD63-positive EVs (**Figure 7B**). Similarly, we observed minimal co-localization of SHH and either CD9 or CD63 by confocal immunofluorescence microscopy (**Figure 7C**), suggesting that most SHH in the 100K fraction is secreted on vesicles distinct from exosomes. To then define the hallmark of SHH-bound vesicles, we immunoisolated SHH positive EVs from the 100K pellet and subjected the bound material to mass spectrometry analysis to identify other components of these EVs (**Figure 7D**). This analysis revealed a unique set of proteins significantly enriched in the SHH fraction, including Ras-related protein Rab-18 (RAB18), Tyrosine-protein kinase receptor UFO (AXL) and Transmembrane emp24 domain-containing protein 10 (TMED10), that have not been reported as major components of exosomes (Welch's t-test, RAB18: p = 0.008, AXL, TMED10: p < 0.001, **Figure 7E, Table S3,** Lotvall et al., 2014). Moreover, the exosomal markers CD63, CD9 and Syntenin were not enriched, while CD81 was present (**Table S3**). By immunoprecipitation of CD63 or SHH, we found that RAB18, AXL, and TMED10 mark a specific EV subtype that is distinct from CD63-positive exosomes (**Figure 7F**), which we label ART-EVs (AXL, RAB18, and TMED10).

CHMP1A is present on ART-EVs

ESCRT components participate in the process of exosome biogenesis, but they are also found associated with EVs in the extracellular environment (Chiasserini et al., 2014). To investigate whether CHMP1A is associated with ART-EVs, we isolated SHH-containing vesicles from the 100K fractions of SVGA WT and *CHMP1A* null cells by immunoprecipitation. WB analysis of the bound fractions revealed the presence of CHMP1A only in the ART-EVs recovered from WT cells, confirming the specificity of the detection (**Figure S12A**). In contrast, AXL and RAB18 were similarly detected in ART-EVs from both WT and *CHMP1A* null cells. High-resolution time-lapse confocal microscopy of the intracellular co-distribution of ectopically expressed SHH and CHMP1A in live SVG-A cells showed that both proteins distributed mostly in independent compartments, but a subset of CHMP1A and SHH structures overlap over time (**Figure S12B, Supplemental Movie**). Taken together, these findings suggest that CHMP1A physically associates with SHH-positive ART-EVs. To confirm that ART-EVs are present in the adult nervous system *in vivo*, we isolated the 100K EV fraction from human adult CSF (collected from a patient with glioblastoma multiforme) and purified SHH-containing vesicles as well as CD63-positive exosomes from the 100K CSF pellet by immunoprecipitation. Pulldown of SHH co-purified AXL and RAB18, which were absent from the CD63-positive exosome fraction (**Figure 7G**), thus confirming the specific protein signature of ART-EVs identified in SVG-A cells. Together, our data strongly suggest that SHH is secreted *in vivo* on a novel EV subtype: ART-EVs.

DISCUSSION

By characterizing *Chmp1a* null mice and *CHMP1A* null human cerebral organoids we show that *CHMP1A* is essential for neural progenitor proliferation and maintenance. Further, we demonstrate that ESCRT-mediated release of extracellular vesicles is impaired in the absence of *CHMP1A* and that this reduces secretion of vesicle-bound SHH, a key driver of progenitor proliferation in the brain. Although loss of an ESCRT-III component could cause widespread defects resulting from impaired vesicle release, essentially all of the neurodevelopmental defects seen in *Chmp1a* null mice (and *CHMP1A* deficient humans) can be ascribed to defective SHH, and we show that defect lies in SHH secretion. We define a new EV subtype, ART-EVs, on which SHH is secreted, and show that ART-EVs exist *in vivo*. Our findings provide evidence for a new mechanism of SHH secretion in vertebrate brain development with broad potential relevance to secretion of growth factors and bioactive molecules in the CNS.

Chmp1a null phenotype is consistent with hypomorphic *Shh* signaling

All of the most obvious neurodevelopmental defects in *Chmp1a* null mice—including a thin cerebral cortex, small basal ganglia, cerebellar hypoplasia, small somatic size, and perinatal lethality—are consistent with partial loss of *Shh*, since these defects have been observed in previous mouse models of decreased *Shh* signaling through hypomorphic alleles (Huang et al., 2007, Chamberlain et al., 2008). In addition, both impaired progenitor maintenance in *CHMP1A* null organoids and microcephaly in *Chmp1a* null mice can be partially rescued by downstream *Shh* signaling activation either chemically or genetically. On the other hand, the lack of digit or spinal cord patterning defects in *Chmp1a* null mice compared to null *Shh* mutations (Zhu and Mackem, 2011, Fuccillo et al., 2006) is consistent with our observed incomplete blockage of Shh

secretion and the observation that spinal cord Shh is secreted on large EVs (Tanaka et al., 2005) whereas depletion of *CHMP1A* specifically impairs secretion of SHH on small EVs (**Figure 6F**). The early lethality of *Chmp1a* null mice precludes identification of additional effects that might reflect regulation of other signaling pathways, and the incomplete correction of defects in some progenitor and differentiation markers in *CHMP1A* null organoids by SAG (**Figure S8**) also leaves open the possibility that *CHMP1A* may regulate other pathways.

Multiple specialized SHH secretion mechanisms

In vivo Hedgehog (Hh) secretion has been studied primarily in *Drosophila* imaginal disk, where the proposed underlying mechanism remains controversial. Matusek et al. showed Hh secretion occurs on larger EVs called ectosomes released from the plasma membrane in an ESCRT-dependent manner (Matusek et al., 2014). In their study, disruption of MVB biogenesis did not impair Hh secretion, suggesting it did not occur via MVB-derived exosomes. In contrast, Parchure et al. reported Hh secretion via ESCRT-mediated exosome-like vesicles derived from MVBs (Parchure et al., 2015). Shh secretion at the embryonic mouse ventral node appears to occur via large, plasma membrane derived EVs (Tanaka et al., 2005), which are not obviously impaired in the absence of *Chmp1a*. These results highlight the complexity and confusion surrounding vesicular Shh secretion, but our data show, for the first time, that Shh secretion on small EVs is essential during brain development and specifically impaired by loss of *CHMP1A*.

SHH secretion via ART-EVs

We report SHH secretion on a novel class of EVs, ART-EVs, defined by marker proteins distinct from classical CD63-positive exosomes. To our knowledge, RAB18, AXL, and

TMED10 have not been previously reported as components of SHH-positive EVs, and so can provide new insights into the mechanism of SHH secretion. RAB18 is a protein with emerging roles in ER to Golgi retrograde trafficking and other cellular trafficking (Vazquez-Martinez et al., 2007, Dejgaard et al., 2008) and LOF mutations in *RAB18* are associated with Warburg Micro syndrome, establishing a critical role of *RAB18* in eye and brain development and neurodegeneration (Bem et al., 2011). The vesicular proteins AXL and TMED10 may function in biogenesis of specific vesicles in SHH producing cells as AXL is a receptor tyrosine kinase expressed at the plasma membrane that is required in microglia for apoptotic cell removal (O'Bryan et al., 1991, Fourgeaud et al., 2016) and TMED10 (TMP21/P23) is a transmembrane protein that is involved in early secretory pathway trafficking and is a member of the Presenilin complex (Blum et al., 1996, Chen et al., 2006). ART-EVs may originate from MVBs, like *bona-fide* exosomes, or may bud from the plasma membrane. Further work is required to determine the similarities and differences between ART-EV and exosome secretion pathways.

CHMP1A regulates secretion of multiple EV subtypes

Previous studies have established important roles for different members of the ESCRT machinery in ILV biogenesis (Colombo et al., 2013; Baietti et al., 2012). We found fewer ILVs within MVBs in the absence of *CHMP1A* and consistent with this phenotype, observed a decrease in exosome secretion. Exosomes have been defined as EVs of MVB origin co-enriched in tetraspannins CD9, CD81 and CD63, and endosome markers TSG101 or Syntenin (Lotvall et al., 2014). However, in our experimental system, we observed reduced secretion of some, but not all exosome markers, indicating the existence of a heterogeneous exosomal population among EVs. This idea is supported by our immunoprecipitation assay, in which only residual amounts

of CD63 were co-isolated with CD9 by anti-CD9 antibodies, and vice-versa (**Figure 7B**), even though both CD63 and CD9 are canonical exosome markers. This finding supports previous work suggesting that exosomes are heterogeneous with respect to their size and cargo, that cells contain distinct MVBs, and that ILVs of the same MVB display different structures and compositions (Colombo et al., 2013, Bobrie et al., 2012, van Niel et al., 2001, Fevrier and Raposo, 2004, Mobius et al., 2002, White et al., 2006). With these results in mind, it is reasonable to suggest that decreased ILV count in *CHMP1A* null MVBs underlies reduction of both SHH positive ART-EVs and CD63-positive exosomes.

Many potential EVs function in the CNS

Whereas the developmental defects caused by the absence of *CHMP1A*—microcephaly, cerebellar hypoplasia, and short stature—highlight the importance and widespread function of EV-mediated cellular communication during development, the persistence of ART-EV's in the adult human CSF suggests that there may be continued requirements for EV-mediated growth factor secretion in adult brain. The widespread distribution of MVBs along dendrites of pyramidal neurons in the cerebral cortex hints at complex forms of cellular communication, perhaps involving retrograde synaptic signaling. Moreover, there is evidence that EV secretion may be hijacked during the pathologic spread of Tau protein that may underlie neuronal degeneration (Asai et al., 2015). In providing the first animal model with specific defects in EV function in the CNS, we provide a potential tool to assess the functions of EVs in these diverse and fundamental processes.

ACKNOWLEDGMENTS

We thank patients and their families for their participation, Jen Partlow for collecting patient MRIs, Brenda Barry for coordinating skin fibroblast collection, Margaret Thompson for *Chmp1a* GT mouse line generation, Stan Hollenberg for CHMP1A antibody, Corey Harwell for *mNG-SHH* plasmid, Adrian Salic for *SHH* plasmid, and Chad Cowan and Kirin Musunuru for CRISPR plasmids. We thank Maria Ericsson, Louise Trakimas, and Elizabeth Benecchi for TEM sample preparation and imaging. We thank Bill Fowle for SEM sample preparation and imaging. This work was supported by NIH R01 NS088566 and the New York Stem Cell Foundation (M.K.L); M.K.L. is a New York Stem Cell Foundation – Robertson Investigator. CAW was supported by R01 NS35129 from the NINDS, and MEC by F30 MH102909. CAW is an Investigator of the Howard Hughes Medical Institute. RG was supported by the IdEx Université de Strasbourg via the French National Research Agency (ANR) as part of the program “investissements d'avenir” and the ATIP-Avenir program. The authors have no financial disclosures to report.

AUTHOR CONTRIBUTIONS

MEC planned the work, conducted experiments, and wrote the manuscript. CAW directed the study and wrote the manuscript. CD and RG designed and performed experiments on EVs and edited the manuscript. FMJ and GAL cultured organoids and performed and analyzed RNA-seq. ETL cultured and sequenced iPSCs. VG and DMG bred *Chmp1a* GT and Ptch KO mouse lines. DMG performed Tbr2 staining and weighed some mouse brains. EY interpreted MRIs. HGWL and MLC collected human choroid plexus. ETW collected human CSF. FD analyzed mass spectrometry. CSX and SP performed FIB-SEM. TS, WAL, MKL, GM, TK, DH, HH, and SC supervised and provided scientific input. All authors read and approved the manuscript.

REFERENCES

Antonucci, F., Turola, E., Riganti, L., Caleo, M., Gabrielli, M., Perrotta, C., Novellino, L., Clementi, E., Giussani, P., Viani, P., et al. (2012). Microvesicles released from microglia stimulate synaptic activity via enhanced sphingolipid metabolism. The EMBO Journal 31, 1231–1240.

Arlotta, P., Molyneaux, B.J., Chen, J., Inoue, J., Kominami, R., and Macklis, J.D. (2005). Neuronal subtype-specific genes that control corticospinal motor neuron development in vivo. Neuron *45*, 207–221.

Asai, H., Ikezu, S., Tsunoda, S., Medalla, M., Luebke, J., Haydar, T., Wolozin, B., Butovsky, O., Kügler, S., and Ikezu, T. (2015). Depletion of microglia and inhibition of exosome synthesis halt tau propagation. Nature Neuroscience *18*, 1584–1593.

Baietti, M.F., Zhang, Z., Mortier, E., Melchior, A., Degeest, G., Geeraerts, A., Ivarsson, Y., Depoortere, F., Coomans, C., Vermeiren, E., et al. (2012). Syndecan-syntenin-ALIX regulates the biogenesis of exosomes. Nat Cell Biol *14*, 677–685.

Bem, D., Yoshimura, S.-I., Nunes-Bastos, R., Bond, F.C., Bond, F.F., Kurian, M.A., Rahman, F., Handley, M.T.W., Hadzhiev, Y., Masood, I., et al. (2011). Loss-of-function mutations in RAB18 cause Warburg micro syndrome. Am. J. Hum. Genet. *88*, 499–507.

Blum, R., Feick, P., Puype, M., Vandekerckhove, J., Klengel, R., Nastainczyk, W., and Schulz, I. (1996). Tmp21 and p24A, two type I proteins enriched in pancreatic microsomal membranes, are members of a protein family involved in vesicular trafficking. J. Biol. Chem. *271*, 17183–17189.

Bobrie, A., Colombo, M., Krumeich, S., Raposo, G., and Théry, C. (2012). Diverse subpopulations of vesicles secreted by different intracellular mechanisms are present in exosome preparations obtained by differential ultracentrifugation. Journal of Extracellular Vesicles *1*, 834.

Budnik, V., Ruiz-Cañada, C., and Wendler, F. (2016). Extracellular vesicles round off communication in the nervous system. Nat. Rev. Neurosci. 17, 160–172.

Campbell, C., Beug, S., Nickerson, P.E.B., Peng, J., Mazerolle, C., Bassett, E.A., Ringuette, R., Jama, F.A., Morales, C., Christ, A., et al. (2016). Sortilin regulates sorting and secretion of Sonic hedgehog. Journal of Cell Science *129*, 3832–3844.

Carapito, C., Burel, A., Guterl, P., Walter, A., Varrier, F., Bertile, F., and Van Dorsselaer, A. (2014) MSDA, a proteomics software suite for in-depth Mass Spectrometry Data Analysis using grid computing. *Proteomics* **14**, 1014-1019

Carlton, J.G., Caballe, A., Agromayor, M., Kloc, M., and Martin-Serrano, J. (2012). ESCRT-III governs the Aurora B-mediated abscission checkpoint through CHMP4C. Science 336, 220–225.

Chamberlain, C.E., Jeong, J., Guo, C., Allen, B.L., and McMahon, A.P. (2008). Notochord-derived Shh concentrates in close association with the apically positioned basal body in neural target cells and forms a dynamic gradient during neural patterning. Development *135*, 1097–1106.

Charron, F., Stein, E., Jeong, J., McMahon, A.P., and Tessier-Lavigne, M. (2003). The morphogen sonic hedgehog is an axonal chemoattractant that collaborates with netrin-1 in midline axon guidance. Cell 113, 11–23.

Chen, F., Hasegawa, H., Schmitt-Ulms, G., Kawarai, T., Bohm, C., Katayama, T., Gu, Y., Sanjo, N., Glista, M., Rogaeva, E., et al. (2006). TMP21 is a presenilin complex component that modulates gamma-secretase but not epsilon-secretase activity. Nature *440*, 1208–1212.

Chiasserini, D., van Weering, J.R.T., Piersma, S.R., Pham, T.V., Malekzadeh, A., Teunissen, C.E., de Wit, H., and Jiménez, C.R. (2014). Proteomic analysis of cerebrospinal fluid extracellular vesicles: A comprehensive dataset. Journal of Proteomics *106*, 191–204.

Cohen, M., Kicheva, A., Ribeiro, A., Blassberg, R., Page, K.M., Barnes, C.P., and Briscoe, J. (2015). Ptch1 and Gli regulate Shh signalling dynamics via multiple mechanisms. Nat Comms 6, 6709.

Colombo, M., Moita, C., van Niel, G., Kowal, J., Vigneron, J., Benaroch, P., Manel, N., Moita, L.F., Théry, C., and Raposo, G. (2013). Analysis of ESCRT functions in exosome biogenesis, composition and secretion highlights the heterogeneity of extracellular vesicles. Journal of Cell Science 126, 5553–5565.

Corrales, J.D., Blaess, S., Mahoney, E.M., and Joyner, A.L. (2006). The level of sonic hedgehog signaling regulates the complexity of cerebellar foliation. Development 133, 1811–1821.

Corrales, J.D., Rocco, G.L., Blaess, S., Guo, Q., and Joyner, A.L. (2004). Spatial pattern of sonic hedgehog signaling through Gli genes during cerebellum development. Development 131, 5581–5590.

Cox, J., Hein, M. Y., Luber, C. A., Paron, I., Nagaraj, N., and Mann, M. (2014) Accurate proteome-wide label-free quantification by delayed normalization and maximal peptide ratio extraction, termed MaxLFQ. *Mol Cell Proteomics* **13**, 2513-2526

Dahmane, N., and Ruiz i Altaba, A. (1999). Sonic hedgehog regulates the growth and patterning of the cerebellum. Development 126, 3089–3100.

Dejgaard, S.Y., Murshid, A., Erman, A., Kizilay, O., Verbich, D., Lodge, R., Dejgaard, K., Ly-Hartig, T.B.N., Pepperkok, R., Simpson, J.C., et al. (2008). Rab18 and Rab43 have key roles in ER-Golgi trafficking. Journal of Cell Science *121*, 2768–2781.

Février, B., and Raposo, G. (2004). Exosomes: endosomal-derived vesicles shipping extracellular messages. Curr. Opin. Cell Biol. *16*, 415–421.

Fourgeaud, L., Través, P.G., Tufail, Y., Leal-Bailey, H., Lew, E.D., Burrola, P.G., Callaway, P., Zagórska, A., Rothlin, C.V., Nimmerjahn, A., et al. (2016). TAM receptors regulate multiple features of microglial physiology. Nature *532*, 240–244.

Frühbeis, C., Fröhlich, D., Kuo, W.P., Amphornrat, J., Thilemann, S., Saab, A.S., Kirchhoff, F., Möbius, W., Goebbels, S., Nave, K.-A., et al. (2013). Neurotransmitter-triggered transfer of exosomes mediates oligodendrocyte-neuron communication. PLoS Biol 11, e1001604.

Fuccillo, M., Joyner, A.L., and Fishell, G. (2006). Morphogen to mitogen: the multiple roles of hedgehog signalling in vertebrate neural development. Nat. Rev. Neurosci. *7*, 772–783.

Goodrich, L.V., Milenkovic, L., Higgins, K.M., and Scott, M.P. (1997). Altered neural cell fates and medulloblastoma in mouse patched mutants. Science *277*, 1109–1113.

Greig, L.C., Woodworth, M.B., Galazo, M.J., Padmanabhan, H., and Macklis, J.D. (2013). Molecular logic of neocortical projection neuron specification, development and diversity. Nat. Rev. Neurosci. 14, 755–769.

Harwell, C.C., Parker, P.R.L., Gee, S.M., Okada, A., McConnell, S.K., Kreitzer, A.C., and Kriegstein, A.R. (2012). Sonic Hedgehog Expression in Corticofugal Projection Neurons Directs Cortical Microcircuit Formation. Neuron 73, 1116–1126.

Howard, T.L., Stauffer, D.R., Degnin, C.R., and Hollenberg, S.M. (2001). CHMP1 functions as a member of a newly defined family of vesicle trafficking proteins. Journal of Cell Science 114, 2395–2404.

Huang, X., Litingtung, Y., and Chiang, C. (2007). Region-specific requirement for cholesterol modification of sonic hedgehog in patterning the telencephalon and spinal cord. Development 134, 2095–2105.

Jarnuczak, A. F., and Vizcaino, J. A. (2017) Using the PRIDE Database and ProteomeXchange for Submitting and Accessing Public Proteomics Datasets. *Curr Protoc Bioinformatics* **59**, 13 31 11-13 31 12

Kim D, Pertea G, Trapnell C, Pimentel H, Kelley R, Salzberg SL. TopHat2: accurate alignment of transcriptomes in the presence of insertions, deletions and gene fusions. (2011). Genome Biology, 14:R36.

Koles, K., Nunnari, J., Korkut, C., Barria, R., Brewer, C., Li, Y., Leszyk, J., Zhang, B., and Budnik, V. (2012). Mechanism of evenness interrupted (Evi)-exosome release at synaptic boutons. J. Biol. Chem. 287, 16820–16834.

Korkut, C., Ataman, B., Ramachandran, P., Ashley, J., Barria, R., Gherbesi, N., and Budnik, V. (2009). Trans-synaptic transmission of vesicular Wnt signals through Evi/Wntless. Cell 139, 393–404.

Korkut, C., Li, Y., Koles, K., Brewer, C., Ashley, J., Yoshihara, M., and Budnik, V. (2013). Regulation of postsynaptic retrograde signaling by presynaptic exosome release. Neuron 77, 1039–1046.

Kowal, J., Arras, G., Colombo, M., Jouve, M., Morath, J.P., Primdal-Bengtson, B., Dingli, F., Loew, D., Tkach, M., and Théry, C. (2016). Proteomic comparison defines novel markers to characterize heterogeneous populations of extracellular vesicle subtypes. Proceedings of the National Academy of Sciences *113*, E968–E977.

Lachenal, G., Pernet-Gallay, K., Chivet, M., Hemming, F.J., Belly, A., Bodon, G., Blot, B., Haase, G., Goldberg, Y., and Sadoul, R. (2011). Release of exosomes from differentiated neurons and its regulation by synaptic glutamatergic activity. Mol. Cell. Neurosci. 46, 409–418.

Langmead B, Salzberg S. Fast gapped-read alignment with Bowtie 2. (2012). Nature Methods, 9:357-359.

Lee, J.-A., Beigneux, A., Ahmad, S.T., Young, S.G., and Gao, F.-B. (2007). ESCRT-III dysfunction causes autophagosome accumulation and neurodegeneration. Curr. Biol. *17*, 1561–1567.

Lee, W.-C.A., Bonin, V., Reed, M., Graham, B.J., Hood, G., Glattfelder, K., and Reid, R.C. (2016). Anatomy and function of an excitatory network in the visual cortex. Nature.

Lizarraga, S.B., Margossian, S.P., Harris, M.H., Campagna, D.R., Han, A.-P., Blevins, S., Mudbhary, R., Barker, J.E., Walsh, C.A., and Fleming, M.D. (2010). Cdk5rap2 regulates centrosome function and chromosome segregation in neuronal progenitors. Development 137, 1907–1917.

Lötvall, J., Hill, A.F., Hochberg, F., Buzás, E.I., Di Vizio, D., Gardiner, C., Gho, Y.S., Kurochkin, I.V., Mathivanan, S., Quesenberry, P., et al. (2014). Minimal experimental requirements for definition of extracellular vesicles and their functions: a position statement from the International Society for Extracellular Vesicles. Journal of Extracellular Vesicles 3.

Lun, M.P., Johnson, M.B., Broadbelt, K.G., Watanabe, M., Kang, Y.J., Chau, K.F., Springel, M.W., Malesz, A., Sousa, A.M.M., Pletikos, M., et al. (2015a). Spatially Heterogeneous Choroid Plexus Transcriptomes Encode Positional Identity and Contribute to Regional CSF Production. Journal of Neuroscience 35, 4903–4916.

Matusek, T., Wendler, F., Polès, S., Pizette, S., D'Angelo, G., Fürthauer, M., and Thérond, P.P. (2014). The ESCRT machinery regulates the secretion and long-range activity of Hedgehog. Nature 516, 99–103.

McCullough, J., Colf, L.A., and Sundquist, W.I. (2013). Membrane fission reactions of the mammalian ESCRT pathway. Annu. Rev. Biochem. *82*, 663–692.

Möbius, W., Ohno-Iwashita, Y., van Donselaar, E.G., Oorschot, V.M.J., Shimada, Y., Fujimoto, T., Heijnen, H.F.G., Geuze, H.J., and Slot, J.W. (2002). Immunoelectron microscopic localization of cholesterol using biotinylated and non-cytolytic perfringolysin O. J. Histochem. Cytochem. *50*, 43–55.

Mochida, G.H., Ganesh, V.S., de Michelena, M.I., Dias, H., Atabay, K.D., Kathrein, K.L., Huang, H.-T., Hill, R.S., Felie, J.M., Rakiec, D., et al. (2012). CHMP1A encodes an essential regulator of BMI1-INK4A in cerebellar development. Nature Genetics 44, 1260–1264.

Nielsen, C.M., and Dymecki, S.M. (2010). Sonic hedgehog is required for vascular outgrowth in the hindbrain choroid plexus. Dev. Biol. 340, 430–437.

O'Bryan, J.P., Frye, R.A., Cogswell, P.C., Neubauer, A., Kitch, B., Prokop, C., Espinosa, R., Le Beau, M.M., Earp, H.S., and Liu, E.T. (1991). axl, a transforming gene isolated from primary human myeloid leukemia cells, encodes a novel receptor tyrosine kinase. Molecular and Cellular Biology *11*, 5016–5031.

Pan, B.T., Teng, K., Wu, C., Adam, M., and Johnstone, R.M. (1985). Electron microscopic evidence for externalization of the transferrin receptor in vesicular form in sheep reticulocytes. J. Cell Biol. 101, 942–948.

Panáková, D., Sprong, H., Marois, E., Thiele, C., and Eaton, S. (2005). Lipoprotein particles are required for Hedgehog and Wingless signalling. Nature *435*, 58–65.

Parchure, A., Vyas, N., Ferguson, C., Parton, R.G., and Mayor, S. (2015). Oligomerization and endocytosis of Hedgehog is necessary for its efficient exovesicular secretion. Mol. Biol. Cell *26*, 4700–4717.

Roelink, H., Porter, J.A., Chiang, C., Tanabe, Y., Chang, D.T., Beachy, P.A., and Jessell, T.M. (1995). Floor plate and motor neuron induction by different concentrations of the amino-terminal cleavage product of sonic hedgehog autoproteolysis. Cell 81, 445–455.

Stryke, D., Kawamoto, M., Huang, C.C., Johns, S.J., King, L.A., Harper, C.A., Meng, E.C., Lee, R.E., Yee, A., L'Italien, L., et al. (2003). BayGenomics: a resource of insertional mutations in mouse embryonic stem cells. Nucleic Acids Res. 31, 278–281.

Tanaka, Y., Okada, Y., and Hirokawa, N. (2005). FGF-induced vesicular release of Sonic hedgehog and retinoic acid in leftward nodal flow is critical for left-right determination. Nature 435, 172–177.

Théry, C., Amigorena, S., Raposo, G., and Clayton, A. (2006). Isolation and characterization of exosomes from cell culture supernatants and biological fluids. Curr Protoc Cell Biol *Ch 3*, 3.22.

Tietje, A., Maron, K.N., Wei, Y., and Feliciano, D.M. (2014). Cerebrospinal fluid extracellular vesicles undergo age dependent declines and contain known and novel non-coding RNAs. PLoS ONE 9, e113116.

van Niel, G., Raposo, G., Candalh, C., Boussac, M., Hershberg, R., Cerf-Bensussan, N., and Heyman, M. (2001). Intestinal epithelial cells secrete exosome-like vesicles. Gastroenterology *121*, 337–349.

Vazquez-Martinez, R., Cruz-Garcia, D., Duran-Prado, M., Peinado, J.R., Castaño, J.P., and Malagon, M.M. (2007). Rab18 inhibits secretory activity in neuroendocrine cells by interacting with secretory granules. Traffic *8*, 867–882.

Veres, A., Gosis, B.S., Ding, Q., Collins, R., Ragavendran, A., Brand, H., Erdin, S., Cowan, C.A., Talkowski, M.E., and Musunuru, K. (2014). Low incidence of off-target mutations in individual CRISPR-Cas9 and TALEN targeted human stem cell clones detected by whole-genome sequencing. Cell Stem Cell *15*, 27–30.

Vyas, N., Walvekar, A., Tate, D., Lakshmanan, V., Bansal, D., Cicero, A.L., Raposo, G., Palakodeti, D., and Dhawan, J. (2014). Vertebrate Hedgehog is secreted on two types of extracellular vesicles with different signaling properties. Sci. Rep. 4, 7357.

Wechsler-Reya, R.J., and Scott, M.P. (1999). Control of neuronal precursor proliferation in the cerebellum by Sonic Hedgehog. Neuron 22, 103–114.

White, I.J., Bailey, L.M., Aghakhani, M.R., Moss, S.E., and Futter, C.E. (2006). EGF stimulates annexin 1-dependent inward vesiculation in a multivesicular endosome subpopulation. The EMBO Journal *25*, 1–12.

Wieczorek, S., Combes, F., Lazar, C., Giai Gianetto, Q., Gatto, L., Dorffer, A., Hesse, A. M., Coute, Y., Ferro, M., Bruley, C., and Burger, T. (2017) DAPAR & ProStaR: software to perform statistical analyses in quantitative discovery proteomics. *Bioinformatics* **33**, 135-136

Wilson, N.H., and Stoeckli, E.T. (2013). Sonic hedgehog regulates its own receptor on postcrossing commissural axons in a glypican1-dependent manner. Neuron 79, 478–491.

Xu, C. S. et. al. Enhanced FIB-SEM Systems for Large-Volume 3D Imaging, eLife 2017 May; doi: 10.7554/eLife.25916

Zeng, X., Goetz, J.A., Suber, L.M., Scott, W.J., Schreiner, C.M., and Robbins, D.J. (2001). A freely diffusible form of Sonic hedgehog mediates long-range signalling. Nature *411*, 716–720.

Zhou, P., Porcionatto, M., Pilapil, M., Chen, Y., Choi, Y., Tolias, K.F., Bikoff, J.B., Hong, E.J., Greenberg, M.E., and Segal, R.A. (2007). Polarized signaling endosomes coordinate BDNF-induced chemotaxis of cerebellar precursors. Neuron 55, 53–68.

Zhu, J., and Mackem, S. (2011). Analysis of mutants with altered shh activity and posterior digit loss supports a biphasic model for shh function as a morphogen and mitogen. Dev. Dyn. *240*, 1303–1310.

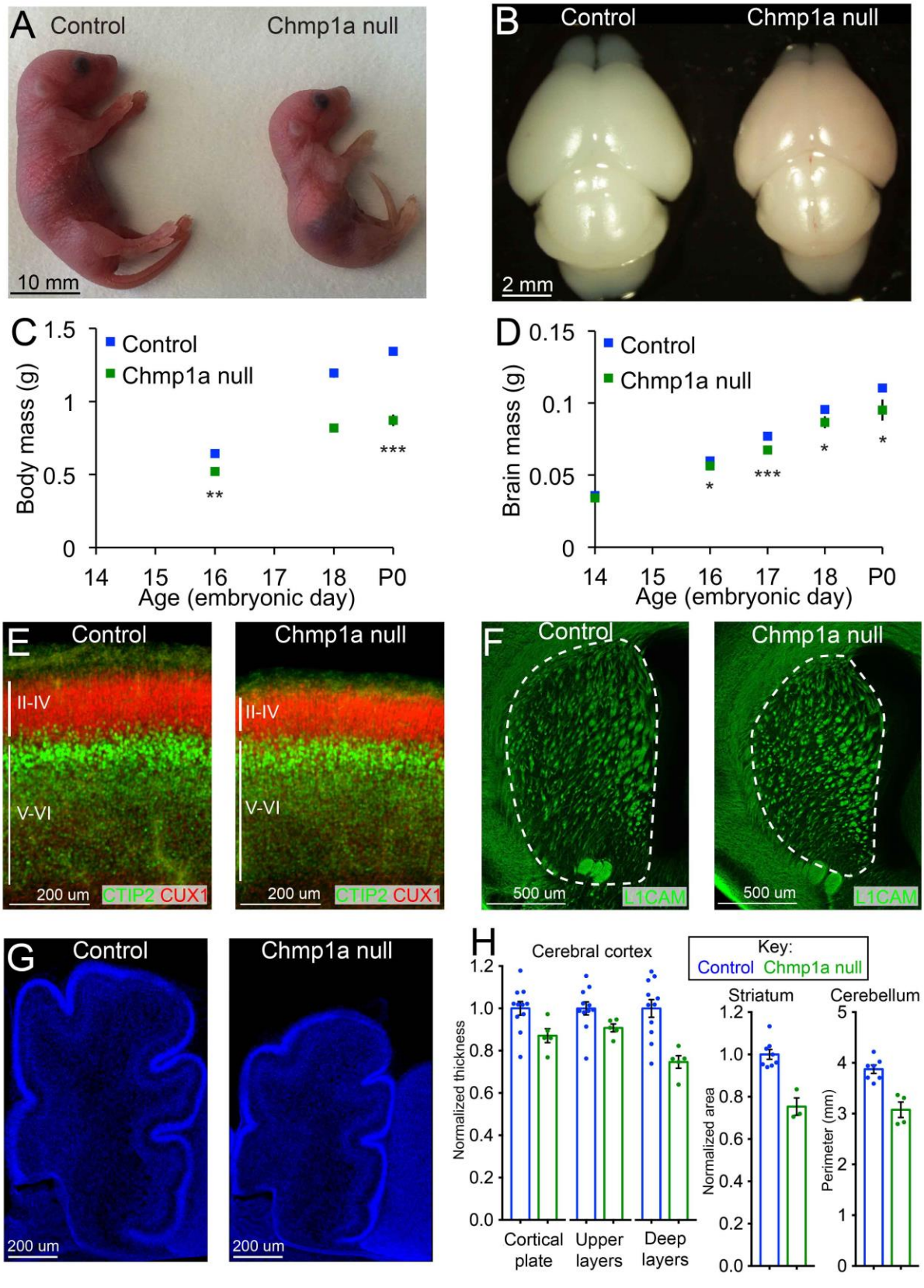
A
Control
Chmp1a null
10 mm
B
Control
Chmp1a null
2 mm
C
Control
Chmp1a null
Body mass (g)
1.5
1
0.5
0
**
***
14
15
16
17
18
P0
Age (embryonic day)
D
Control
Chmp1a null
Brain mass (g)
0.15
0.1
0.05
0
*
***
*
*
14
15
16
17
18
P0
Age (embryonic day)
E
Control
Chmp1a null
II-IV
V-VI
200 um
CTIP2 CUX1
F
Control
Chmp1a null
500 um
L1CAM
G
Control
Chmp1a null
200 um
H
Cerebral cortex
Key:
Control Chmp1a null
Striatum
Cerebellum
Normalized thickness
1.2
1.0
0.8
0.6
0.4
0.2
0.0
Cortical plate
Upper layers
Deep layers
Normalized area
Perimeter (mm)
5
4
3
2
1
0

Figure 1: *Chmp1a* is essential for brain development in mice

(A) P0 *Chmp1a* null pups are smaller than littermate controls. (B) P0 *Chmp1a* null pups have smaller brains than controls. Note smaller olfactory bulbs and shorter A-P length of the cortex. (C) Body mass is reduced in *Chmp1a* null embryos, E16.5: Control: n=7, *Chmp1a* null: n=2; E18.5: Control: n=6, *Chmp1a* null: n=1; P0: Control: n=17, *Chmp1a* null: n=2. (D) Brain mass is reduced in *Chmp1a* null embryos, E14.5: Control: n=10, *Chmp1a* null: n=5; E16.5: Control: n=6, *Chmp1a* null: n=2; E17.5: Control: n=23, *Chmp1a* null: n=4; E18.5: Control: n=20, *Chmp1a* null: n=3; P0: Control: n=9, *Chmp1a* null: n=3. (E) The cortical plate is 13% thinner in *Chmp1a* null embryos at E18.5, Control: n=11, *Chmp1a* null: n=5. (F) Striatum area is reduced by 25% at E18.5 in *Chmp1a* null embryos compared to controls, Control: n=8, *Chmp1a* null: n=3. (G) P0 midline section shows cerebellar hypoplasia (18% reduction) in *Chmp1a* null pups compared to control littermates, Control: n=7, *Chmp1a* null: n=4. (H) Quantification of E-G. Two-tailed t-test, * $p < 0.05$, ** $p < 0.01$, *** $p < 0.001$.

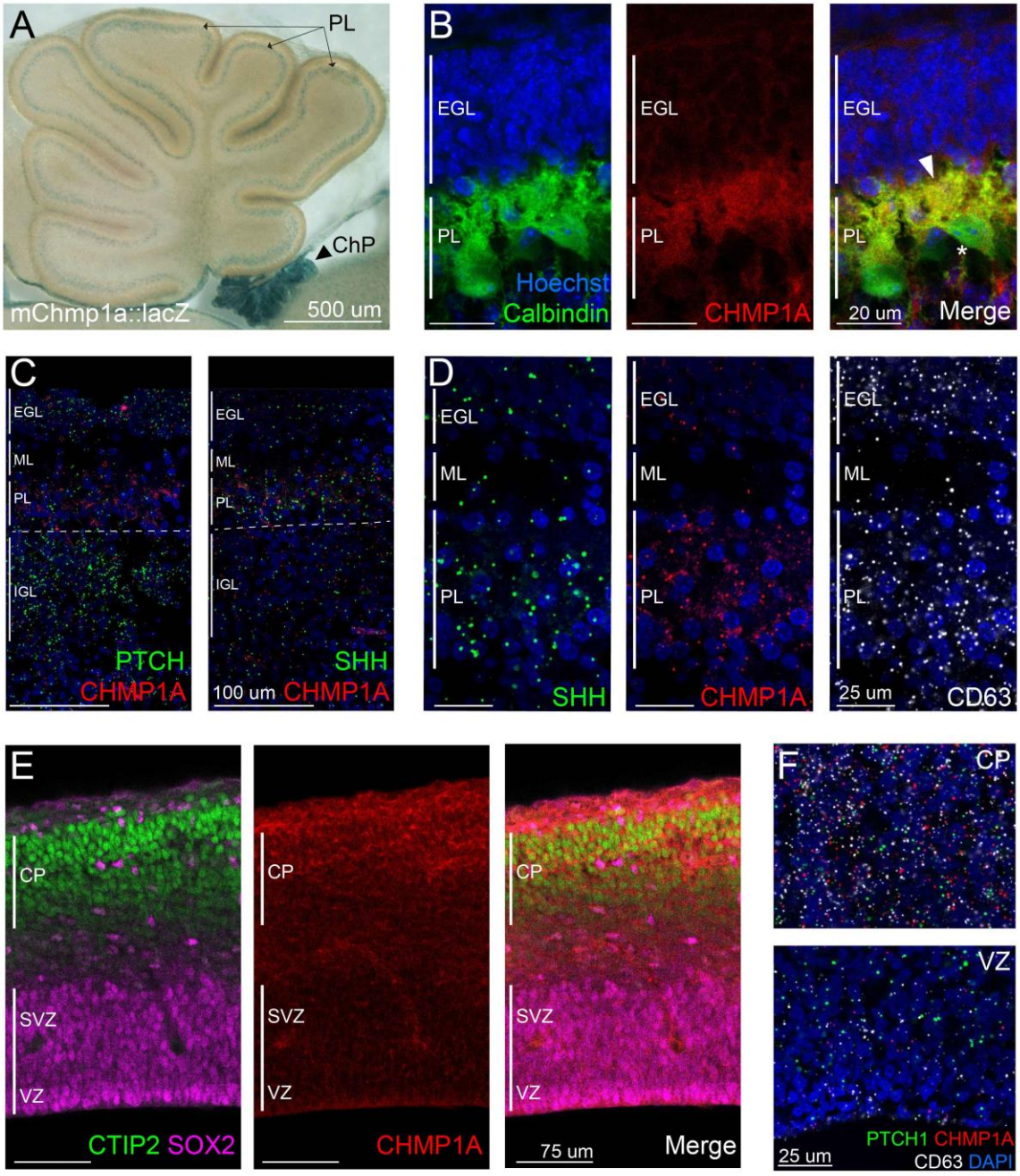
A
PL
ChP
mChmp1a::lacZ
500 um
B
EGL
PL
Hoechst
Calbindin
CHMP1A
20 um
Merge
C
ML
IGL
PTCH
SHH
100 um
D
25 um
CD63
E
CP
SVZ
VZ
CTIP2 SOX2
75 um
F
PTCH1 CHMP1A
CD63 DAPI

Figure 2: Chmp1a is expressed in neurons and ChP epithelial cells in developing brain

(A) In P4 cerebellum, Chmp1a-LacZ is detected in Purkinje cell layer and absent from EGL. LacZ is also strongly expressed in hindbrain ChP. (B) Chmp1a immunoreactivity in cerebellar Purkinje cells (P4). Merge of Calbindin and Chmp1a highlights Chmp1a in Purkinje cell cytoplasm and dendrites (arrowhead) with absence in the nucleus (asterisk). (C) RNAscope expression of *CHMP1A*, *SHH*, and *PTCH* in developing human cerebellum. (D) RNAscope expression of *CHMP1A*, *SHH*, and *CD63* in developing human cerebellum. (E) Mouse Chmp1a protein is expressed in post-mitotic neurons (Ctip2) in the cerebral cortex but not in progenitors (Sox2) at E14.5. (E) *CHMP1A*, *PTCH*, and *CD63* expression in developing human cortex by RNAscope shows analogous localization. All panels are representative image of ≥2 experiments.

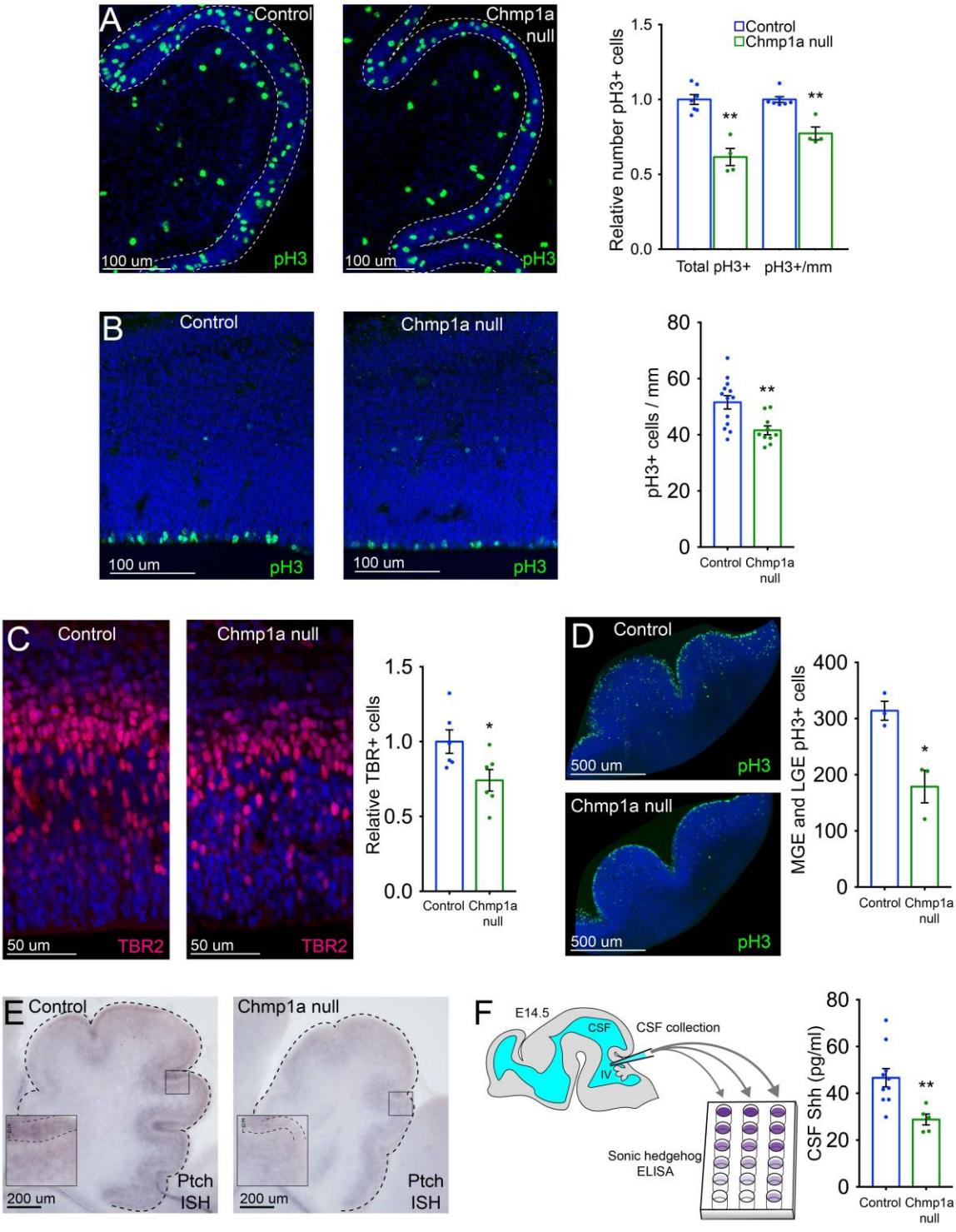
A
Control
Chmp1a null
100 um
pH3
Relative number pH3+ cells
Control
Chmp1a null
Total pH3+
pH3+/mm
B
pH3+ cells / mm
Control
Chmp1a null
C
TBR2
Relative TBR+ cells
D
500 um
MGE and LGE pH3+ cells
E
Ptch ISH
200 um
F
E14.5
CSF
CSF collection
IV
Sonic hedgehog ELISA
CSF Shh (pg/ml)

Figure 3: *Chmp1a* is required for progenitor proliferation in telencephalon and hindbrain

(A) *Chmp1a* null P0 pups have 38% fewer mitotic GCPs than control littermates, Control: n=7, *Chmp1a* null: n=4. (B) 19% reduction in pH3 positive mitotic cortical progenitors at E14.5 *Chmp1a* null embryos, Control: n=13, *Chmp1a* null: n=10. (C) E13.5 *Chmp1a* null embryos have 26% fewer Tbr2 positive intermediate progenitors than controls, Control: n=6, *Chmp1a* null: n=6. (D) MGE and LGE show 43% fewer pH3 positive mitotic progenitors in *Chmp1a* null embryos, Control: n=3, *Chmp1a* null: n=3. (E) ISH for *Ptch* shows reduced expression in *Chmp1a* null P0 cerebellum. Control: n=4, *Chmp1a* null, n=3. (F) CSF concentration of Shh in 4^{th} ventricle at E14.5 is reduced 38% in *Chmp1a* null embryos, Control: n=10, *Chmp1a* null: n=5. Two-tailed, unpaired t-test, * $p < 0.05$, ** $p < 0.01$.

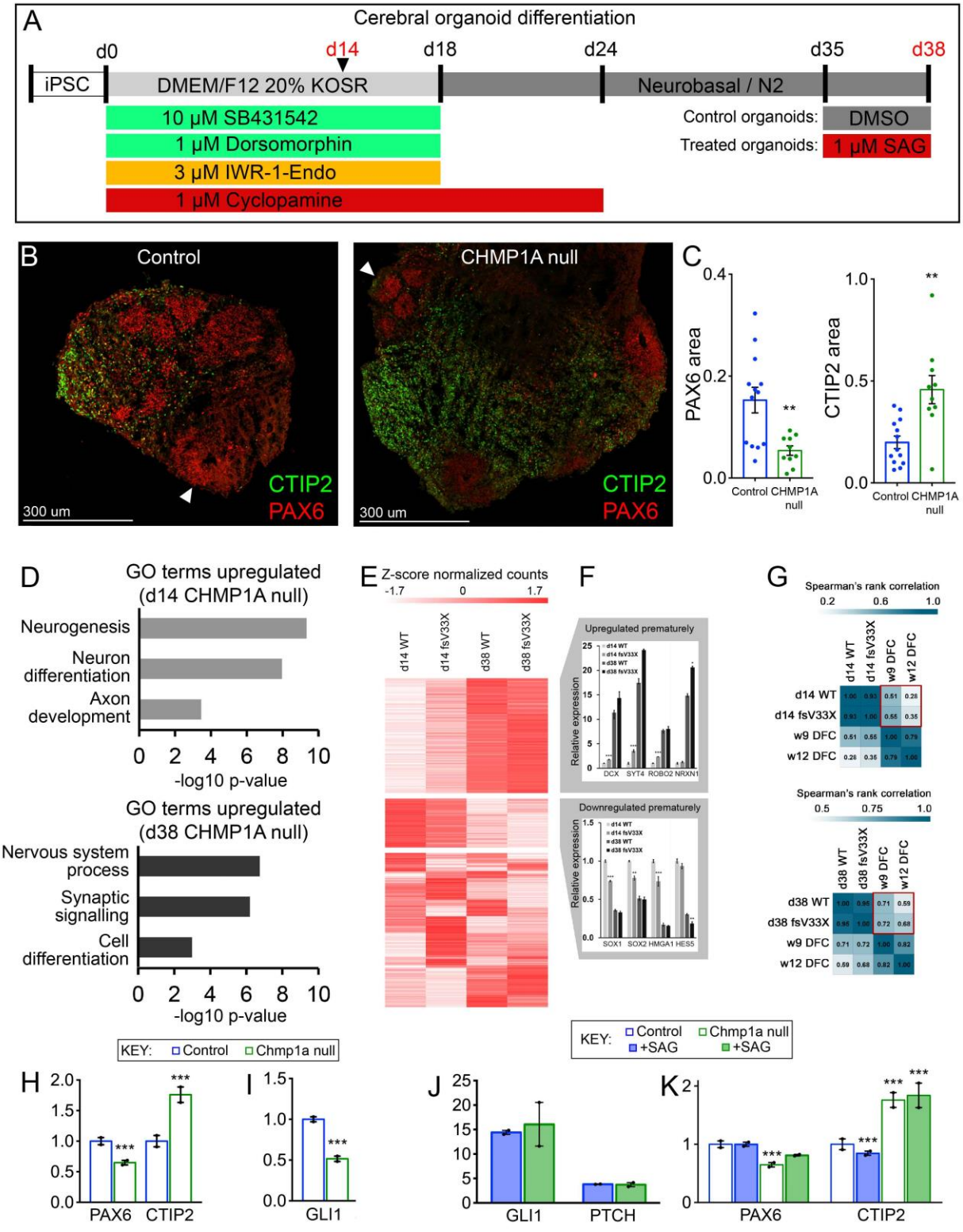
A
Cerebral organoid differentiation
d0
d14
d18
d24
d35
d38
iPSC
DMEM/F12 20% KOSR
Neurobasal / N2
10 µM SB431542
1 µM Dorsomorphin
3 µM IWR-1-Endo
1 µM Cyclopamine
Control organoids:
DMSO
Treated organoids:
1 µM SAG
B
Control
CHMP1A null
CTIP2
PAX6
300 um
C
PAX6 area
CTIP2 area
Control
CHMP1A null
D
GO terms upregulated (d14 CHMP1A null)
Neurogenesis
Neuron differentiation
Axon development
-log10 p-value
GO terms upregulated (d38 CHMP1A null)
Nervous system process
Synaptic signalling
Cell differentiation
E
Z-score normalized counts
d14 WT
d14 fsV33X
d38 WT
d38 fsV33X
F
Upregulated prematurely
Downregulated prematurely
Relative expression
DCX
SYT4
ROBO2
NRXN1
SOX1
SOX2
HMGA1
HES5
G
Spearman's rank correlation
w9 DFC
w12 DFC
KEY:
Control
Chmp1a null
+SAG
H
I
PAX6
CTIP2
GLI1
J
PTCH
K

Figure 4: *CHMP1A* is essential for progenitor proliferation in human cerebral organoids

(A) Human cerebral organoid differentiation protocol. (B) Organoids contain cortical progenitors (red, immunostained for PAX6, arrowheads) surrounded by postmitotic neurons (green, immunostained for CTIP2). (C) PAX6 area is decreased and CTIP2 area is increased in *CHMP1A* null organoids, Control: n=13, *Chmp1a* null: n=10. (D) GO pathway enrichment analysis. (E) RNA sequencing reveals clusters of genes up- and down-regulated in *CHMP1A* null organoids. (F) Expression of proliferative marker genes is decreased in *CHMP1A* null organoids while expression of differentiation and post-mitotic neuron markers is increased. (G) Comparison of organoid gene expression profiles to expression profiles of human fetal cortex. (H) Decreased *PAX6* expression and increased *CTIP2* expression by RNA sequencing at day 38 in *CHMP1A* null organoids. (I) Decreased *GLI1* expression in *CHMP1A* null iPSCs. (J) SAG treatment of organoids induces *GLI1* and *PTCH* expression. (K) SAG treatment partially rescues decreased *PAX6* expression in *CHMP1A* null organoids. C, J: Two-tailed, unpaired t-test; F, H, I, K: DESeq2 adjusted p-value; * $p < 0.05$, ** $p < 0.01$, *** $P < 0.001$.

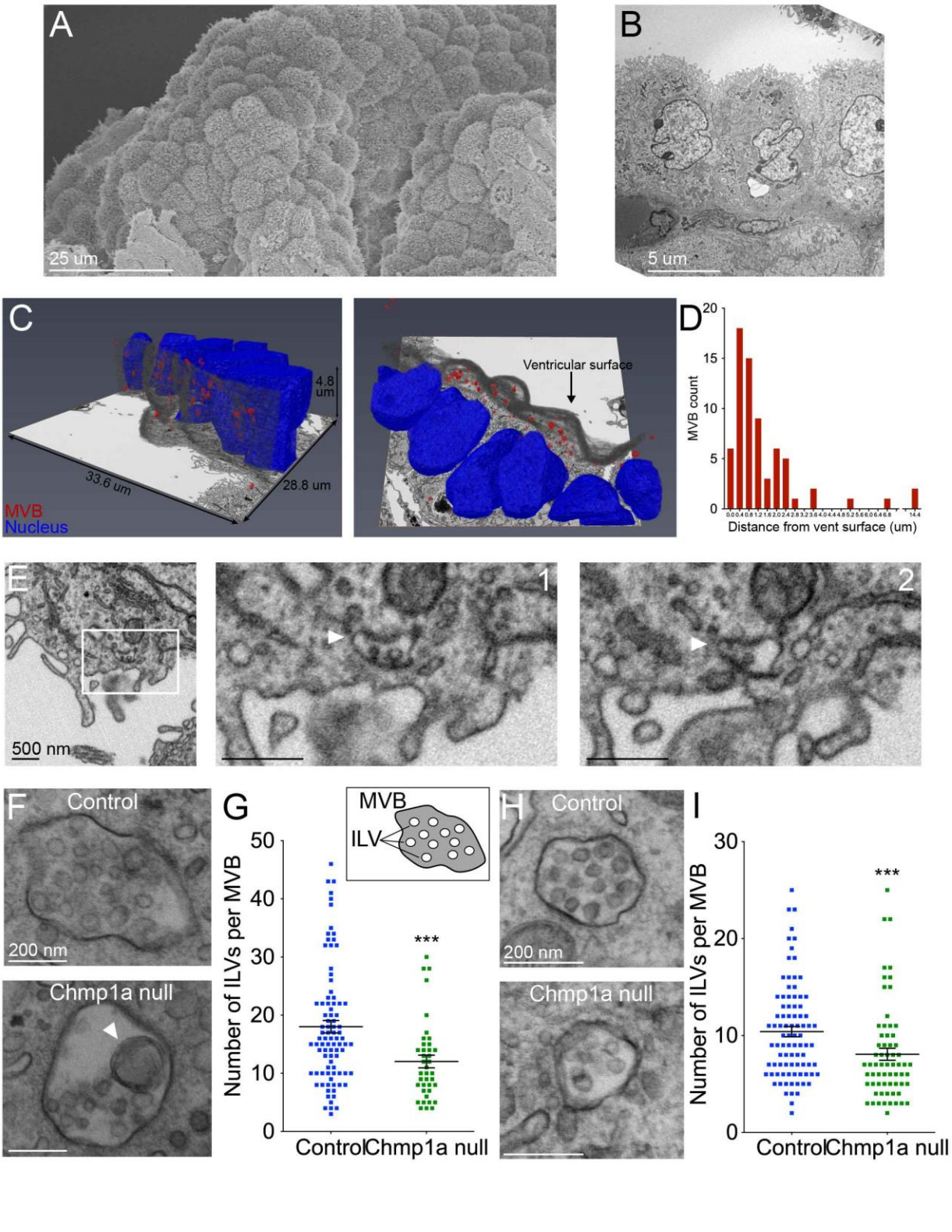
A
25 um
B
5 um
C
4.8 um
33.6 um
28.8 um
MVB
Nucleus
Ventricular surface
D
MVB count
Distance from vent surface (um)
E
500 nm
1
2
F
Control
200 nm
Chmp1a null
G
MVB
ILV
Number of ILVs per MVB
***
Control
Chmp1a null
H
Control
200 nm
Chmp1a null
I
Number of ILVs per MVB
***
Control
Chmp1a null

Figure 5: *Chmp1a* is essential for ILV formation in developing mouse brain

(A) SEM of mouse embryonic hindbrain ChP. (B) TEM of mouse embryonic hindbrain ChP. (C) FIB-SEM of mouse ChP revealed accumulation of MVBs near epithelial cell ventricular surface. (D) Quantification of MVB distribution within epithelial cells. (E) MVB fused with plasma membrane of ChP epithelial cell (arrowhead). (F) Fewer ILVs in *Chmp1a* null ChP MVBs and abnormally large ILVs (arrowhead). (G) Quantification of (F), Control: n=88 MVBs (7 embryos), *Chmp1a* null: n=39 MVBs (2 embryos). (H) Fewer ILVs in *Chmp1a* null Purkinje cells. (I) Quantification of (H), Control: n=88 MVBs (6 embryos), *Chmp1a* null: n=74 MVBs (2 embryos). G, I: Mann-Whitney test, *** $p < 0.001$.

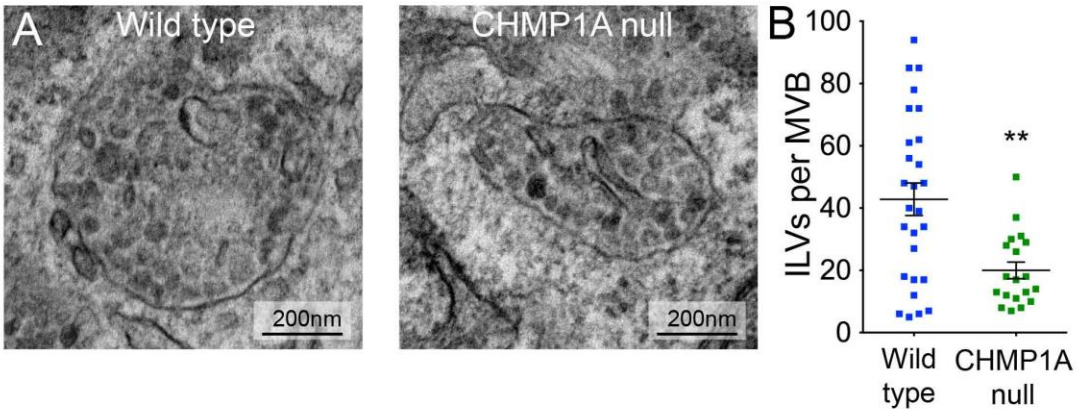
A
Wild type
200nm
CHMP1A null
200nm
B
ILVs per MVB
100
80
60
40
20
0
**
Wild type
CHMP1A null

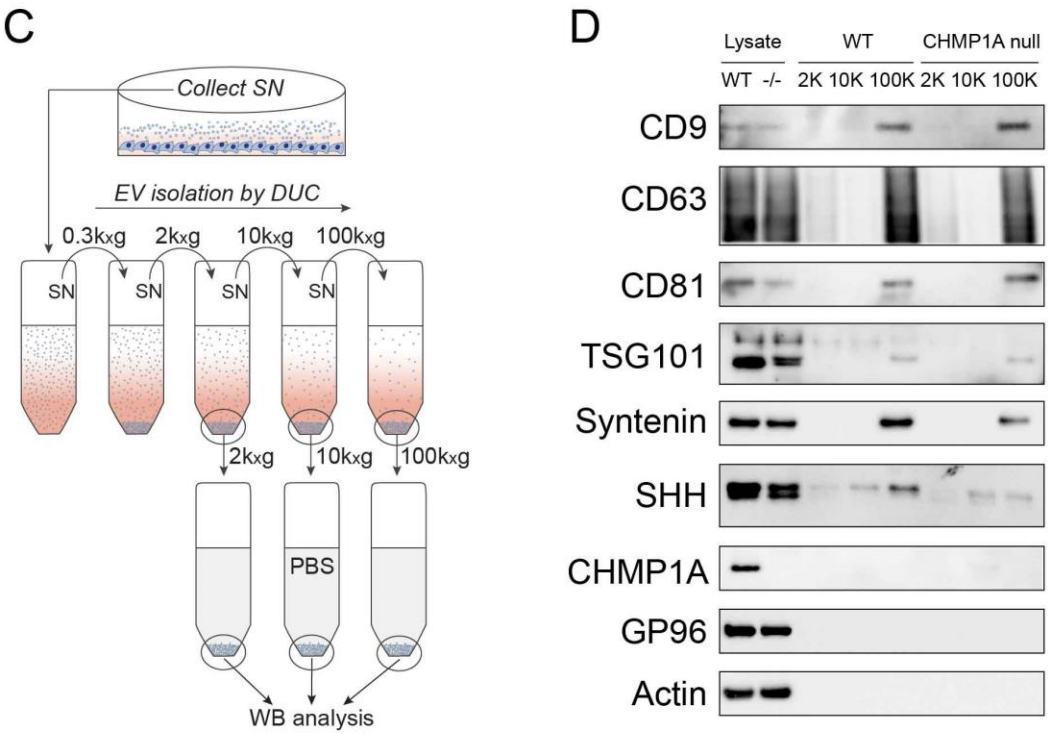
C
Collect SN
EV isolation by DUC
0.3kxg
2kxg
10kxg
100kxg
SN
SN
SN
SN
2kxg
10kxg
100kxg
PBS
WB analysis
D
Lysate
WT
CHMP1A null
WT -/-
2K 10K 100K 2K 10K 100K
CD9
CD63
CD81
TSG101
Syntenin
SHH
CHMP1A
GP96
Actin

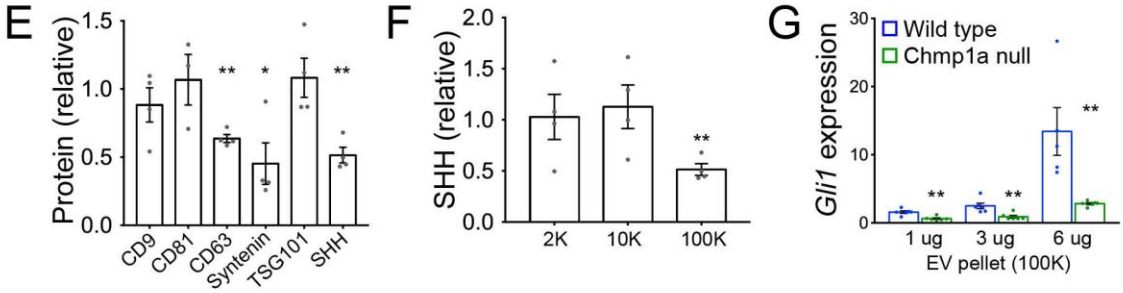
E
Protein (relative)
1.5
1.0
0.5
0.0
**
*
**
CD9
CD81
CD63
Syntenin
TSG101
SHH
F
SHH (relative)
2.0
1.5
1.0
0.5
0.0
**
2K
10K
100K
G
Gli1 expression
30
20
10
0
Wild type
Chmp1a null
**
**
**
1 ug
3 ug
6 ug
EV pellet (100K)

Figure 6: *CHMP1A* depletion decreases secretion of SHH and exosomes *in vitro*

(A) Decreased ILV formation in MVBs of *CHMP1A* null SVG-A cells compared to WT (TEM). (B) Quantification of (A), Control: n=41, *CHMP1A* null: n=46. (C) EV isolation procedure (Kowal et al, 2016). (D) Representative WB analysis of isolated EVs (2K, 10K, 100K pellets) from WT and *CHMP1A* null SVG-A cells expressing SHH. Blot shows EV-specific markers (CD9, CD63, CD81, Syntenin, TSG101), EV-excluded markers (GP96, Actin), CHMP1A, and SHH. (E) Quantification of (D), Wild type: n=4, *CHMP1A* null, n=4. (F) Quantification of SHH WB signals in the 2K, 10K and 100K fractions, Wild type: n=4, *CHMP1A* null, n=4. (G) *Gli1* induction in NIH3T3 cells induced by 100K pellet from SHH transfected SVG-A cells. 1ug, 3ug: Wild type: n=6, *CHMP1A* null: n=6. 6ug: Wild type: n=5, *CHMP1A* null, n=6. B: Mann-Whitney test, ** $p < 0.01$. E-G: two-tailed, unpaired t-test, * $p < 0.05$, ** $p < 0.01$.

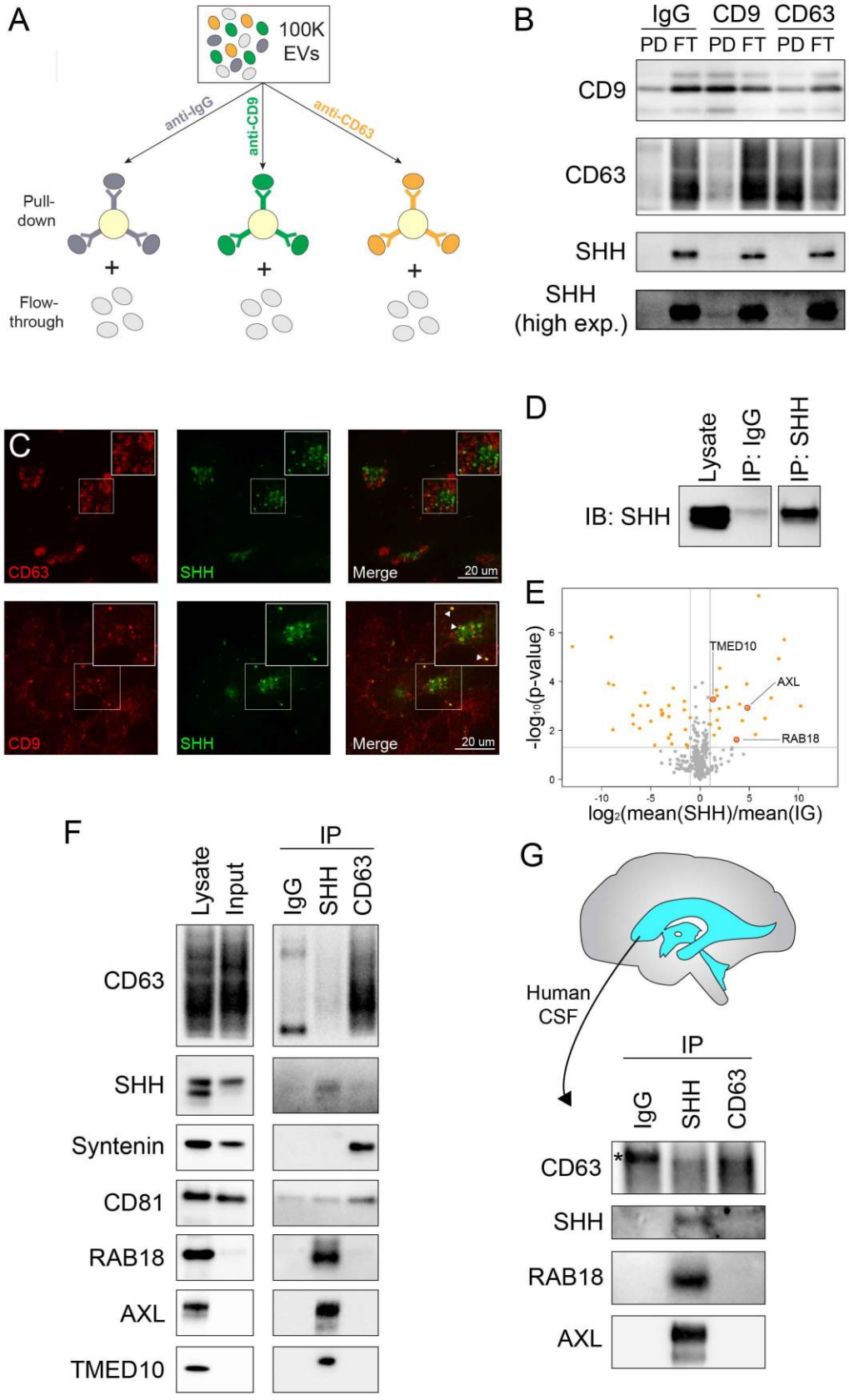
A
100K EVs
anti-IgG
anti-CD9
anti-CD63
Pull-down
Flow-through
B
IgG
CD9
CD63
PD FT PD FT PD FT
CD9
CD63
SHH
SHH (high exp.)
C
CD63
SHH
Merge
20 um
CD9
SHH
Merge
20 um
D
Lysate
IP: IgG
IP: SHH
IB: SHH
E
TMED10
AXL
RAB18
-log10(p-value)
log2(mean(SHH)/mean(IG))
F
Lysate
Input
IP
IgG
SHH
CD63
CD63
SHH
Syntenin
CD81
RAB18
AXL
TMED10
G
Human CSF
IP
IgG
SHH
CD63
CD63
SHH
RAB18
AXL

Figure 7: SHH is secreted on a novel EV subtype, ART-EVs

(A) Scheme of exosome isolation from the 100K pellet by immunoprecipitation using beads coupled to CD9, CD63 antibodies or mouse Pan-IgG antibodies. Both bound (pull-down) and unbound (flow-through) material was recovered. (B) Representative WB of the bound and unbound fractions from exosome immunoisolation, probed with antibodies against CD9, CD63 and SHH. Note that most SHH does not co-purify with exosomes, but remains in the FT fraction. (C) Immunostaining of exosomal markers CD9 or CD63 in cells ectopically expressing mNeonGreen-SHH. (D) SHH-positive vesicles were purified from the 100K pellet by immunoisolation using anti-SHH antibodies. (E) Peptides enriched in EVs isolated by SHH immunoisolation. (F) Immunoisolated SHH-positive vesicles and CD63-positive exosomes were subjected to WB analysis, confirming the exclusive presence of RAB18, AXL and TMED10, in purified SHH-vesicles. In contrast, Syntenin is only found on CD63-positive exosomes, while CD81 is present on both type of vesicles. (G) SHH- and CD63-positive vesicles from the 100K pellet were immunoisolated from human CSF and subjected to WB analysis, confirming the exclusive presence of RAB18 and AXL on ART-EVs *in vivo*. * indicates non-specific band.

Supplemental Information

STAR METHODS

CONTACT FOR REAGENT AND RESOURCE SHARING

Further information and requests for resources and reagents should be directed to and will be fulfilled by Lead Contact, Christopher A. Walsh (christopher.walsh@childrens.harvard.edu).

EXPERIMENTAL MODEL AND SUBJECT DETAILS

Human Samples

Operating under an approved institutional review board (IRB) protocol, normal human choroid plexus was identified and collected at autopsy by pathologists at Boston Children's Hospital.

Operating under an approved institutional review board (IRB) protocol, human CSF was collected by neurologists at Beth Israel Deaconess Medical Center.

Operating under an approved institutional review board (IRB) protocol, GW20 human fetal whole brain tissue was collected at autopsy by pathologists at Beth Israel Deaconess Medical Center.

Animal Use

All animals were cared for humanly and all experiments were approved by Boston Children's Hospital IACUC.

Chmp1a GT mouse generation and mouse breeding

Mouse ES cells with a gene trap cassette inserted into *Chmp1a* were obtained from BayGenomics (B6;129P2-Chmp1a$^{Gt(XC472)Byg}$/Mmucd) and injected into blastocysts of WT mice. Resulting chimeras were out crossed with WT C57/Bl6 mice to generate heterozygous GT mice. Heterozygous GT mice were backcrossed to C57/Bl6 for 7-8 generations. Mouse DNA was genotyped with the following primers: WT primer F: GAGACAGCGGGTCCGTAAC, WT primer R: AACACACACTCGAACCGAAAG, GT primer F: GAGACAGCGGGTCCGTAAC, GT primer R: GGTCCTAGTCGGAGGTCTCG.

Ptch null mouse

Ptch null mouse line (Goodrich et al., 1997) was purchased from Jackson Labs and genotyped according to their protocol.

CHMP1A null cell line generation

Monoclonal SVG-A *CHMP1A* null line and iPSC *CHMP1A* null lines were generated using CRISPR-Cas9 mutagenesis (Veres et al., 2014) Cas9 was expressed from a plasmid encoding Cas9 and GFP (Gift of Chad Cowan and Kirin Musunuru). gRNA targeting *CHMP1A* was expressed from a co-transfected plasmid, *CHMP1A* protospacer sequence: GAAGGACTCCAAGGCGGAGC. GFP positive cells were grown as single colonies isolated and then sequenced to identify homozygous frame shift mutations in *CHMP1A*. Controls were

monoclonal lines from the same experiments shown to WT by Sanger sequencing. Primers used to genotype were F: GAAGACAGACACTGGAGAAAACC R: CAGAAGACAAACCAGGAGAGTCA.

Heterogeneous *CHMP1A* null cell line generation

SVG-A *CHMP1A* null cell line (heterogenous pool of either WT or KO cells) was generated using CRISPR-Cas9 mutagenesis (Veres et al., 2014). Cas9 was expressed from a lentiviral plasmid (Gift of Feng Zhang, MIT) also encoding the far-red fluorescent protein E2-Crimson, the puromycin resistance gene, and gRNA targeting CHMP1A (GAAGGACTCCAAGGCGGAGC). Lentivirus was harvested 48 h after transfecting the Cas9 packaging plasmids together with plasmids encoding HIV Gag-Pol and VSV-G envelope in Hek293T cells using JetPrime (Polyplus transfection) according to the manufacturer's instructions. SVG-A cells were incubated with lentivirus for 24 h in the presence of 1 μg/ml Polybrene (EMD Millipore). 3 days later, cells were exposed to puromycin (2 μg/ml) for one week for selection, after which survivors were bulk sorted by FACS based on high E2-Crimson expression. A KO control cell line was generated using a similar strategy and a lentivirus construct encoding gRNA targeting the luciferase gene (CTTCGAAATGTCCGTTCGGT).

Cell lines and culture conditions

Human brain astroglial cells SVG-A and mouse embryonic fibroblasts NIH3T3 were cultured at 37ºC and 5% CO2 in high-glucose DMEM (Gibco) supplemented with 10% FCS and 1% penicillin-streptomycin. iPSCs (line IMR90-4, from WiCell) were grown on Matrigel (BD) in mTESR media (Stem Cell Tech). MEFs were cultured in DMEM high glucose supplemented with 10% FBS, 1% P/S, and 2 mM L-glutamine.

Cerebral organoid culture and isolation

Cerebral organoids were harvested at 14 days or 38 weeks post differentiation, and generated according to the following method: iPSC colonies were grown on a feeder layer of mouse MEFs (35,000 cells/cm^2) and cultured in W0 medium (DMEM/F12, 20% KOSR, 2mM L-glutamine, 1x NEAA, 1x P/S, 50 μM b-mercaptoethanol (Thermofisher) + 8 ng/ml FGF2 (added fresh daily, Sigma)). After iPSC colonies reached 2-3mm in diameter, they were lifted with a cell scraper and transferred to ultra-low attachment 60mm culture dishes (Corning), containing W0 + 1x sodium pyruvate (Differentiation medium, no FGF2). After 24 hours, initial embryoid bodies are formed and (day 0) 50% of medium was replaced with Differentiation medium + small molecule inhibitors to the following final concentrations: 10 μM SB-431542 (Sigma), 1 μM Dorsomorphin (Sigma), 3 μM IWR-1-Endo (Sigma) and 1 μM Cyclopamine (Sigma). Differentiation medium + small molecules was then replaced every other day. On day 4, 60mm plates containing organoids were placed on a hi/lo rocker inside the incubator. On day 18, medium was replaced with Neurobasal/N2 medium (Neurobasal, 1x N2 supplement, 2 mM L-glutamine, 1x P/S) supplemented with 1 μM Cyclopamine. On day 26 medium was replaced with Neurobasal/N2 medium without cyclopamine. At day 35, organoids were culured in Neurobasal/N2 medium supplemented with 1 μM SAG (treated), or DMSO (control), and refreshed daily. At day 38, for RNA isolation, organoids were isolation in TRIzol (Thermofisher). For immunostainings, organoids were washed twice with PBS and fixed by incubated 10 minutes in 3.8% PFA / PBS. After fixation, organoids were washed three times in 0.1% BSA / PBS. Then organoids were incubated in 15% sucrose / PBS at 4°C for 2 hours, followed by incubation in 30% sucrose / PBS

overnight at 4°C. Using a cut off pipette tip, single organoids were transferred to embedding molds containing Shandon M-1 embedding matrix (Thermofisher) and stored at -80°C.

Generation of *Chmp1a* null MEFs
Chmp1a GT heterozygous mice were crossed and E14-15 embryos were collected. Embryos were decapitated and visceral organs removed. The remaining tissue was dissociated with Trypsin and then plated and maintained in DMEM high glucose supplemented with 10% FBS, 1% P/S, and 2 mM L-glutamine. MEFs were assayed before passage 4.

METHOD DETAILS

pH3 analysis
Matching coronal telencephalon sections at E12.5 or E14.5, or midline sagittal cerebellum sections at P0 were immunostained for pH3. pH3+ cells lining the cortical ventricular surface were counted at E14.5, pH3+ cells in the MGE and LGE were counted at E12.5, and pH3+ cells in the cerebellar EGL were counted at P0.

LacZ staining
Chemical staining for beta-galactosidase activity was performed with the beta-gal staining kit from Invitrogen (K146501). Briefly, tissue was fixed overnight in 2% gluteraldehyde, microtome sectioned (70 uM), and then stained for beta-gal activity according to the kit instructions.

In situ hybridization
In situ hybridization was performed as previously described (Arlotta et al., 2005). *Ptch* in situ probe was a gift from C Cepko and A Joyner. RNA was synthesized with the Megascript kit from Invitrogen. DIG dNTPS and anti-DIG Fab fragments were ordered from Roche.

Mouse embryo CSF collection and SHH ELISA
CSF was collected from the 4th ventricle of E14.5-E15.5 *Chmp1a* null mouse embryos and littermate controls using a pulled micropipette. CSF was centrifuged at 10000 G for 5 minutes and then used in the SHH ELISA. SHH ELISA kit was purchased from R and D systems (MSHH00) and used according to the manufacture's instructions.

Human choroid plexus immunostaining
Choroid plexus tissue was fixed in 4% PFA, frozen, and sectioned at 15 um on a cryostat. Cultured iPSCs were fixed with 4% PFA for 10 minutes at RT. Tissue or cells were permeabilized with 0.04% Tween in PBS and blocked in 0.04% tween, 2.5% donkey serum, and 2.5% goat serum in PBS. Sections or cells were incubated with primary antibody diluting in blocking buffer overnight at 4C. Sections or cells were then stained with Alexa secondary antibodies and Hoechst. Imaging was done on Zeiss 510 confocal microscope.

Mouse brain and human organoid immunostaining
Tissue was fixed overnight at 4 C in 4% PFA and sectioned at 70um using a Vibratome. Antigen retrieval was performed with Retrievagen A. Tissue was permeabilized and blocked in 3% BSA, 0.3% Triton X-100, 0.3% sodium azide in PBS. Primary antibodies were diluted in blocking

buffer and incubated overnight at 4 C. Sections were then stained with Alexa secondary antibodies and Hoechst. Imaging was done on Zeiss 510 confocal microscope.

Two results confirm the specificity of the CHMP1A antibody used for immunostaining (ProteinTech 15761-1-AP). First, immunoblot of *Chmp1a* null MEF cell lysate with this antibody shows no reactivity (**Figure 1B**). Second, tissue sections from *Chmp1a* null mice incubated with this antibody show nearly complete loss of signal (**Figure S3B**).

RNAscope

RNAscope on human fetal brain tissue was performed according to manufacturer's protocol (ACDBio).

RNA sequencing library preparation

Cerebral organoid RNA was isolated according to standard TRIzol protocol. RNA was treated with DNAseI (Roche) according to standard protocol for DNA clean-up in RNA samples. RNA was then isolated by column purification (Zymo RNA clean & concentrator 5) and stored at -80°C. For RNA sequencing, first mRNA was isolated from total RNA using polyA selection Dynabeads mRNA DIRECT Micro Purification Kit (Thermofisher). Library was prepared using strand-specific Ion Total RNA-Seq Kit v2 (Thermofisher) and Ion Xpress RNA-Seq Barcode 1-16 (Thermofisher) to label different samples. Sequencing was done using IonProton sequencer, generating single-end reads of around 100bp in length (Thermofisher).

Mapping of RNA sequencing data

RNA sequencing data was processed using the Tuxedo package. Briefly, samples were mapped using Tophat2 (Kim et al., 2011), using Bowtie2 (Langmead and Salzberg, 2012) as the underlying alignment tool. The iPSC input fastq files consisted of paired end reads with each end containing 100bp for iPSC data. The cerebral organoid input fastq consisted of single-end reads of around 100bp length for cerebral organoid data. The target genome assembly for these samples was GRCh38/UCSC hg38, and Tophat was additionally supplied with the gene annotation of ENSEMBL84 (GRCh38.p5). Reads mapped per exon were counted using HT-Seq count (union mode) and summed per corresponding gene. HT-Seq count output was normalized using DESeq2, and pairwise comparisons were made to determine significant differences in control and *CHMP1A* null iPSCs or cerebral organoids. For generation of heatmaps, z-score was calculated using log-transformed normalized counts. Expression level and fold-change for all mapped transcripts are provided in **Supplemental Table 1**.

GO pathway enrichment analysis

For genes with at least a 2-fold change between wild type and CHMP1a null, enrichment of gene sets for GO- Biological Processes (BP-FAT) and KEGG-pathways was determined by DAVID (Database for Annotation, Visualization and Integrated Discovery) Functional Annotation Clustering (v6.7). For each analysis raw RNAseq read counts were normalized using DEseq2. For week 2 and week 5 respectively, all genes with mean read count >64 and read count >32 were included as background. Clusters of GO-terms and KEGG pathways were manually given a name that best represented all individual GO-term categories within each cluster. The DAVID Functional Annotation Tool provides an 'enrichment score' but does not provide a measure of statistical significance for Functional Annotation Clusters. For each Functional Annotation

Cluster, the benjamini-corrected p-value for the highest-ranking individual GO-term in each cluster is displayed next to the bar graphs. GO analysis results and input gene lists are provided in **Supplemental Table 2**.

For figure 4D, the top 250 differentially expressed genes (DESeq2) were selected at d14 or d38 samples from pairwise comparisons between *CHMP1A* null and control cerebral organoids. Upregulated or downregulated genes were placed into separate gene lists. Analysis was done using Panther Overrepresentation test on GO biological processes with Bonferroni correction. Background gene list consisted of all genes, which had on average 10 counts or more mapped in the analyzed samples. In this analysis, the downregulated genes did not show relevant enrichment for brain related GO terms. For supplemental figure 7C, the analysis was also done according to these parameters. Genes that were already differentially expressed between untreated d38 control and d38 *CHMP1A* null organoids were excluded. The remaining genes were selected by DESeq2 adjusted p-value < 0.01 instead to limit the amount of genes for analysis.

Gene expression correlation human brain and cerebral organoids

Cerebral organoid RNA-seq data was compared to developing human brain RNA-seq data (Brainspan, Allen institute). For Figure 4G, d14 and d38 *CHMP1A* null and control organoids, the top 250 differentially expressed genes (DESeq2) were selected. For supplemental figure 7A / B, genes with adjusted p-value < 0.01 were selected to limit the number of genes for analysis. Their corresponding expression data was acquired from Brainspan data. Cerebral organoids have best correlation with Brainspan week 9 dorsofrontal cortex data (w9 DFC). Several other time-points of DFC data were used to assess temporal identity of organoids. Genes were ranked by their expression level from high to low, using normalized counts for organoid data, and FPKM for Brainspan data. Then, pairwise calculation of Spearman's rank correlation was done for each pair and plotted using multi-experiment viewer.

***Shh* signaling in MEFs**

MEFs from *Chmp1a* null embryos and littermate controls were cultured as described above. The cells were then cultured in 0.5% FBS with 1 uM SAG for 48 hours. Then total RNA was isolated with RNeasy kit (Ambion) and cDNA was created with Superscript III kit (Invitrogen). Taqman qRT-PCR assay was run on StepOnePlus (Applied Biosystems) with probes for Axin2 and Beta-actin to measure gene expression.

Extracellular vesicle isolation

SVG-A cells were either mock-transfected or transfected with a plasmid encoding hSHH using JetPrime according to the manufacturer's instructions. 24 h later, cells were washed once with PBS and cultured for another 48h in media supplemented with exosome-depleted FBS (System Biosciences) instead of normal FBS, before harvesting cells for lysis and supernatants (SN) for EV isolation. EVs were isolated from conditioned media by differential ultracentrifugation as previously described (Kowal et al., 2016). Briefly, SN was centrifuged for 10 min and 300xg to pellet cells and large debris. The SN was transferred to new tubes and further centrifuged at 2,000xg for 20 min to obtain the 2K pellet. The resulting SN was then transferred to ultracentrifuge tubes and centrifuged in an SW28 rotor (Beckman Coulter) for 40 min at 10,000xg (10K pellet) before a final centrifugation at 100,000xg using the same rotor (100K

pellet). Except for the 300xg pellet, all pellets were washed in 5 ml PBS before being recentrifuged at the same speed using a SW55Ti rotor (Beckman Coulter) and finally resuspended in 50 µl cold PBS. All steps were performed at 4°C. The 300xg pellet was pooled with cells harvested from dishes for lysis and WB analysis.

A similar protocol was applied for the isolation of EVs from human CSF (18 mL).

Immunoisolation pull-down assays
2 µg of either anti-CD9 (Milipore), anti-CD63 (Pelicluster), anti-Shh (Abcam) or Mouse IgG antibodies were coupled overnight to 1 mg of magnetic Dynabeads using Dynabeads Antibody coupling kit (Invitrogen) according to the manufacturer's instructions. As described in Kowal et al., 2016, coated beads were washed twice in 1 ml washing buffer (PBS-Tween 0.001%) and incubated overnight using rotation at 4°C with 10 µg of EVs from the 100K pellet resuspended in 500 µl of washing buffer. Beads were washed five times with washing buffer, and, where indicated the unbound material was pooled together with the SN of the washes and centrifuged at 100000xg in a SW55Ti rotor for concentration. Both bound material (PD) and unbound material pellet (FT) were resuspended in 30 µl of 2x SDS-PAGE sample buffer (Bio-Rad) and boiled for 5 min at 95°C prior to loading on gel. For MS analysis, Shh pull-down reaction was scaled-up approximately five times.

Liquid Chromatography-Tandem Mass Spectrometry (LC-MS/MS)
Samples were lysed using Laemmli buffer (10 mM Tris pH 6,8 ; 1mM EDTA ; 5% ß-mercaptoethanol ; 5% SDS ; 10% glycerol) and were homogenized during 40 minutes. Samples were briefly centrifuged and the supernatant was collected leaving the magnetic beads in the tubes thanks to a magnet. Samples were then frozen at -80°C until use. Protein concentrations were determined using the RC-DC protein assay (Bio-Rad, Hercules, USA) according to the manufacturer's instructions using BSA as standard.

50 µL of each sample were concentrated down to 20 µL (SpeedVac, Savant, Thermo Fisher Scientific, Waltham, USA) and heated at 95°C for 5 minutes before being loaded onto an in-house poured 1D SDS-PAGE stacking gel in order to focus proteins into a single "stacked" band. Electrophoresis was performed under a continuous voltage of 50 V for 40 minutes. The proteins were fixed with 50% ethanol and 3% phosphoric acid. After three washes, gels were stained with Colloidal blue.

For each sample, the "stacked" protein-band was excised and cut into four equal pieces. After destaining, DTT reduction and IAM alkylation using an automatic pipetting device (MassPrep, Waters, Milford, MA, USA), proteins were in-gel digested with trypsin (Promega, Madison, WI, USA) overnight at 37°C. Tryptic peptides were extracted first in 60 % acetonitrile/0.1 % formic acid in water for 90 minutes, followed by a second extraction in 100% acetonitrile for 10 minutes, at 450 rpm on an orbital shaker. Acetonitrile was evaporated under vacuum and samples were adjusted to 8µL using 0.1% formic acid before nanoLC-MS/MS analysis.

NanoLC-MS/MS analyses were performed on a nanoACQUITY Ultra-Performance-LC system (UPLC) coupled to a Q-Exactive Plus Orbitrap (Thermo Fisher Scientific) mass spectrometer.

The Q-Exactive Plus Orbitrap mass spectrometer is equipped with a nanoelectrospray ion source. The UPLC system consisted of a solvent degasser nanoflow pump, a thermostat-controlled column oven set to a temperature of 60 °C and a thermostat-controlled autosampler at 10 °C. Mobile phase A (99.9% water and 0.1% FA) and mobile phase B (99.9% acetonitrile and 0.1%FA) were delivered at 450 nL/min by the nanoAcquity. Samples were loaded into a Symmetry C18 precolumn (0.18 x 20 mm, 5 µm particle size, Waters) over 3 minutes in 1% buffer B at a flow rate of 5 µL/min. Sample loading was followed by reverse-phase separation at a flow rate of 450 nL/min using an ACQUITY UPLC® BEH130 C18 separation column (200mm x 75 µm id, 1.7 µm particle size, Waters). The Q-Exactive plus Orbitrap instrument was operated in data-dependent acquisition mode by automatically switching between full MS and consecutive MS/MS acquisitions. Survey full scan MS spectra (mass range 300-1,800) were acquired in the Orbitrap at a resolution of 70,000 at 200 m/z with an automatic gain control (AGC) fixed at 3×10^6 ions and a maximal injection time set to 50 ms. The ten most intense peptide ions in each survey scan with a charge state ≥ 2 were selected for MS/MS. MS/MS spectra were acquired at a resolution of 17,500 at 200 m/z, with a fixed first mass at 100 m/z, AGC was set to 1×10^5, and the maximal injection time was set to 100 ms. Peptides were fragmented in the HCD cell by higher-energy collisional dissociation with a normalized collision energy set to 27. Peaks selected for fragmentation were automatically included in a dynamic exclusion list for 60 s, and peptide match selection was turned on. MS data were saved in RAW file format (Thermo Fisher Scientific) using XCalibur. Raw data collected were processed and converted with MSConvert in .mgf peak list format.

Raw files were processed using MaxQuant (v1.5.5.1). Peak lists were searched using the decoy mode of the Andromeda search engine implemented in MaxQuant against a protein database created using MSDA, our home-developed software suite (Carapito et al., 2014). The database contained human and bovin protein sequences (UniProtKB-SwissProt Taxonomy ID: 9606 and 9913 respectively; 26191 entries), which were downloaded in May 2017. Sequences of common contaminants like keratins and trypsin (247 entries, included in MaxQuant) were finally added to the protein database. Regarding search parameters, MS tolerance was set to 20 ppm for the first search and 4.5 ppm for the main search. A maximum number of 2 missed cleavage was accepted, and carbamidomethylation of cysteine residues was set as fixed modification, while acetylation of protein N-termini and oxidation of methionine residues were set as variable modifications. False discovery rates (FDR) were set to 1% for both peptide spectrum matches (minimum length of 7 amino acids) and proteins. Finally, based on the principle of parsimony, shared peptides between proteins were attributed to the protein with the highest number of assigned peptides. Regarding quantification, data normalisation and estimation of protein abundance was performed using the MaxLFQ (label free quantification) option implemented in MaxQuant (Cox et al., 2014). “Match between runs” was enabled using 0.7 minutes time windows after retention time alignment. MaxLFQ quantification was applied using a minimal ratio count of one. Both unmodified and modified (acetylation of protein N-termini and oxidation of methionine residues) peptides were considered for quantification, but shared peptides were not. All other MaxQuant parameters were set as default. The MaxQuant results were visualized and treated with Prostar software for statistical analysis (Wieczarek et al., 2017). Only proteins with at least three intensity values in at least one of the two groups to be compared were retained. Welch’s t-test was applied to identify differentially expressed proteins at a p-value <0.05.

Western blotting

SVG-A cells were lysed in a buffer containing 50 mM Tris-HCl (pH 7.5), 0.3 M NaCl, 0.5% Triton X-100, and protease inhibitors (1x, Roche) for 20 min on ice, with intense vortexing at the begging and end of the incubation. Lysates were cleared by centrifugation at 18000xg for 15 min at 4^{o}C before transferring the supernatant to new tubes. The protein content in the lysates and in the purified EV fractions was measured in the presence of 0.2% SDS, using Pierce BCA protein assay kit (Thermo Fisher Scientific) according to the manufacturer's instructions. For each WB, 20 µg of lysates or 3 µg of EV pellets were loaded on 4-12% NuPAGE Bis-Tris Protein Gels (Invitrogen) and ran under non-reducing conditions. Transfer was done using iBlot2 NC Transfer stacks (Invitrogen) prior to primary antibody incubation overnight at 4^{o}C. Membranes were revealed by chemiluminescence using Clarity or Clarity Max Western ECL Blotting Substrates (Bio-Rad) and images were acquired using ChemiDoc Touch system (Bio-Rad).

Immunostaining and Time-lapse microscopy

SVG-A cells were grown on glass coverslips in 24-well plates for 24 h, prior to transfection with a plasmid encoding for mNeonGreen-Shh using JetPrime according to the manufacturer's instructions. 24 h later, cells were washed once with PBS and fixed for 20 min at room temperature (RT) with 4% paraformaldehyde. Blocking and permeabilization was done with PBS-0.1% Triton X-100 and 0.5% BSA for 30 min. Cells were incubated with the indicated primary antibodies for 2 h at RT, followed by incubation with secondary antibodies for 45 min, diluted in blocking buffer (Alexa Fluor Donkey anti-Mouse-647 or Alexa Fluor Donkey anti-Rabbit-647). Coverslips were mounted with Fluoromount (Sigma-Aldrich). Image acquisition was performed using an AxioObserver.Z1 inverted microscope (Zeiss) mounted with a spinning disc head (Yokogawa), a back-illuminated EMCCD camera (Evolve, Photometrics) and a X100, 1.45 NA oil objective (Zeiss) controlled by Visiview v.3.3.0 software (Visitron Systems). For live cell imaging, cells were co-transfected as described above with mNG-SHH and TagRFP-CHMP1A on coverslips in 6-well plates, and imaged 48h later in cell media at 37^{o}C and 5% CO_2 in a dark incubation chamber. Z-stacks of 0.5 µm interval with two-channel detection were acquired every 5 s, and time-lapse images were analyzed with Imaris v.9.0.1 (Bitplane).

SHH signaling and RT-qPCR

NIH3T3 cells were seeded in 48-well plates to confluency and cultured for 24 h in complete DMEM. Cells were then grown in media without FBS for another 24h, prior to incubation for another 48 hours with the indicated amounts of SHH-containing 100K vesicles or mock (PBS). As positive control of pathway activation, cells were incubated with 250nM SAG reconstituted in DMSO (Abcam) or DMSO as control. Total RNA was isolated using ReliaPrep RNA Cell Miniprep System (Promega) and cDNA was created with SuperScript VILO Master Mix (Invitrogen) by manufacturer's instructions. qRT-PCR assay was run on the CFX96 Touch Real-Time PCR Detection System and gene expression was measured with primers specific for the SHH downstream target gene *GLI1* (F: TTGGATTGAACATGGCGTCT and R: CCTTTCTTGAGGTTGGGATGA). Gene expression is shown as fold change relative to mock-treated cells, following normalization to housekeeping gene *RPL27* (F: GTCGAGATGGGCAAGTTCAT and R: GCTTGGCGATCTTCTTCTTG).

Cytokinesis analysis

Mouse cortex at E14.5 and cultured iPSCs were fixed in 4% PFA. Cortical ventricular surface or cultured iPSCs were immunostained with antibodies against aurora A kinase, pH3 and Hoechst. Aurora A labels the midbody in anaphase through telophase while pH3 labels histones from prophase through metaphase. A high-power field was imaged and the number of pH3 positive early mitotic cells and the number of aurora A positive late mitotic cells was counted. The ratio of midbodies to pH3 positive cells was calculated as measure of cytokinesis duration.

Electron microscopy

Embryonic mouse choroid plexus and P0 mouse cerebellum was fixed in 2.5% Glutaraldehyde and 2% Paraformaldehyde in 0.1 M sodium cacodylate buffer (pH 7.4) at 4C overnight. 70 um thick tissue sections were cut on a vibratome. Sections were washed in 0.1 M cacodylate buffer and postfixed with 1% Osmiumtetroxide (OsO4) and 1.5% Potassiumferrocyanide (KFeCN6) for 1 hour, washed in water 3x and incubated in 1% aqueous uranyl acetate for 1 hour followed by 2 washes in water and subsequent dehydration in grades of alcohol (10 min each; 50%, 70%, 90%, 2x 10 min 100%). The samples were then infiltrated for 15 min in a 1:1 mixture of propyleneoxide and TAAB Epon (Marivac Canada Inc. St. Laurent, Canada). The samples were embedded in drops of TAAB Epon between two sheets of aclar plastic (Electron Microscopy Sciences) and polymerized at 60C for 48 hours. Ultrathin sections (about 80 nm) were cut on a Reichert Ultracut-S microtome, placed onto copper grids, stained with uranyl acetate and lead citrate and examined in a JEOL 1200EX transmission electron microscope. Images were recorded with an AMT 2k CCD camera.

SEM samples were postfixed in 1.0% osmium tetroxide in 0.1M cacodylate buffer (pH 7.4) for 1 hour at room temperature. Following postfixation, the samples were rinsed with buffer then dehydrated through a graded series of ethanol. The specimens were then critical point dried with CO2 using a Samdri PVT-3 critical point dryer (Tousimis Corp. Rockville, MD). The specimens were attached to specimen mounts using conductive adhesive tabs, coated with 5nm platinum using a Cressington 208HR sputter coater (Cressington Scientific Instruments, Ltd. Walford, UK). SEM images were collected on a Hitachi S-4800 at Northeastern University.

For FIB-SEM, Durcupan embedded sample was first mounted on a Cu stud, then imaged by a customized Zeiss NVision40 FIB-SEM system previously described (Xu, et al., 2017). The sample was biased at 400 V to improve image contrast by filtering out secondary electrons. The block face was imaged by a 1 nA electron beam with 1.5 keV landing energy at 500 kHz. The x-y pixel resolution was set at 8 nm. A subsequently applied focused Ga^+ beam of 27 nA at 30 keV strafed across the top surface and ablated away 2 nm of the surface. The newly exposed surface was then imaged again. The ablation – imaging cycle continued about once every minute for couple days. The sequence of acquired images formed a raw imaged volume, followed by post processing of image registration and alignment using a Scale Invariant Feature Transform (SIFT) based algorithm. The aligned stack was binned by a factor of 4 along z to form a final isotropic volume of 28x34x5 μm^3 with 8x8x8 nm^3 voxels, which can be viewed in arbitrary orientations.

QUANTIFICATION AND STATISTICAL ANALYSIS

In all analyses, mean values are presented for pooled data and errors bars are SEM.

Relative intensities of the WB bands were quantified using ImageLab software version 5.2.1 (Bio-Rad) using Volume Tools, global background subtraction and linear regression method. Band intensities of WT samples were set as 100% and used to calculate the protein levels in the KO samples, plotted as percentage of WT (**Figures 6E, 6F**).

For mass-spec experiments, Welch's t-test was applied to identify differentially expressed proteins at a p-value <0.05 (**Figure 7E, Table 2**).

For RNA-sequencing of cerebral organoids, the significance of gene expression differences was calculated with the DESeq2 adjusted p-value. For GO pathway analysis, each Functional Annotation Cluster, the benjamini-corrected p-value for the highest-ranking individual GO-term in each cluster is displayed next to the bar graphs. For comparison between organoid gene expression and human developing cortex, pairwise calculation of Spearman's rank correlation was done for each comparison.

For all other quantifications, statistical significance was determined using a two-tailed, unpaired t-test or a Mann-Whitney test. All counts of ILVs per MVB failed the D'Agostino and Pearson normality test ($p < 0.01$). As a result, the nonparametric Mann-Whitney test was used to test significance of ILV per MVB differences. Statistical analyses were performed using GraphPad Prism version 7.

DATA AND SOFTWARE AVAILABILITY

RNA sequencing data will be deposited in GEO.
Proteomics data have been deposited in ProteomeXchange (PXD007990).

KEY RESOURCES TABLE

REAGENT or RESOURCE	SOURCE	IDENTIFIER
Antibodies		
Rat anti L1CAM	Millipore	MAB5272
Mouse anti TUJ1	Biolegend	801201
Rabbit anti CHMP1A (WB)	Stan Hollenberg	
Rabbit anti CHMP1A (IHC)	ProteinTech	15761-1-AP
Mouse anti Beta actin	Abcam	AC-15
Mouse anti Calbindin	Abcam	AF2E5
Mouse anti AQP1	Santa Cruz	SC25287
Rat anti CTIP2	Abcam	AB18465
Goat anti SOX2	Santa Cruz	SC17330
Mouse anti CD63	Pelicluster	M1544
Rabbit anti CUX1	Santa Cruz	SC13024 M-222
Rat anti phospho Histone H3	Sigma	H9908
Rabbit anti SHH	Abcam	AB73958
Rabbit anti Cleaved caspase 3	Abcam	AB13847
Mouse anti Beta catenin	BD	610153
Rabbit anti Atypical PKC	Santa Cruz	SC216
Mouse anti Aurora A	BD	611082
Mouse anti CD9	Millipore	CBL162
Rabbit anti CD9	Abcam	ab92726

Mouse anti CD81	Santa Cruz	sc-166029
Mouse anti CD81	Abcam	ab59477
Mouse anti TSG101	Abcam	ab83
Mouse anti TSG101	Thermo Fisher	MA1-23296
Rabbit anti Syntenin	Abcam	ab133267
Rat anti GP96	Enzo Life Sciences	ADI-SPA-850-F
Rabbit anti AXL	Cell Signaling	8661S
Rabbit anti RAB18	MilliporeSigma	SAB4200173
Rabit anti TMED10	Sigma-Aldrich	HPA047139
Goat anti SHH	Santa Cruz	sc-1194
Rabbit anti PAX6	Covance	PRB-278P-100
Bacterial and Virus Strains		
None		
Biological Samples		
Human CSF	Eric Wong	
Human choroid plexus	Hart Lidov	
Chemicals, Peptides, and Recombinant Proteins		
Smoothened agonist (SAG)	Abcam	ab142160
Critical Commercial Assays		
Dynabeads Antibody Coupling Kit	Invitrogen	14311D
RNAscope	ACDBio	
Shh ELISA	R&D Systems	MSHH00
Deposited Data		
RNA sequencing	GEO	
Proteomics	ProteomeXchange	PXD007990
Experimental Models: Cell Lines		
SVG-A	T Kirchhausen	
iPSC (IMR90)	WiCell	
NIH3T3	ATCC	
Chmp1a null MEF	This paper	
Experimental Models: Organisms/Strains		
Chmp1a gene trap mouse	This paper	
Ptch mutant mouse	JAX	
Oligonucleotides		
CHMP1A gRNA	This paper	
Luciferase gRNA	This paper	
Gli1 qPCR F primer	This paper	
Gli1 qPCR R primer	This paper	
Rpl27 qPCR F primer	This paper	
Rpl27 qPCR R primer	This paper	
Chmp1a WT F primer	This paper	
Chmp1a GT F primer	This paper	
Chmp1a WT R primer	This paper	
Chmp1a GT R primer	This paper	
Recombinant DNA		
Mouse *Ptch in situ* probe	Constance Cepko	

mNG-SHH	Corey Harwell	
TagRFP-CHMP1A	This paper	
Cas9 GFP	Kirin Musunuru	
Cas9-E2-Crimson	Feng Zhang	
gRNA backbone	Kirin Musunuru	
RNAscope probe Hs CD63	ACDBio	505901
RNAscope probe Hs SHH	ACDBio	600951
RNAscope probe Hs PTCH	ACDBio	422161
RNAscope probe Hs CHMP1A	ACDBio	505911
Software and Algorithms		
Visiview	Visitron Systems	
Imaris	Bitplane	
ImageLab	Bio-Rad	
CFX Manager	Bio-Rad	
ImageJ	NIH	
XCalibur	Thermo	
MSConver		
MaxQuant		
Prostar		
Prism 7	GraphPad	
Other		
None		

Supplemental Movie 1: Live-cell imaging showing partial co-distribution of intracellular CHMP1A and SHH signal over time

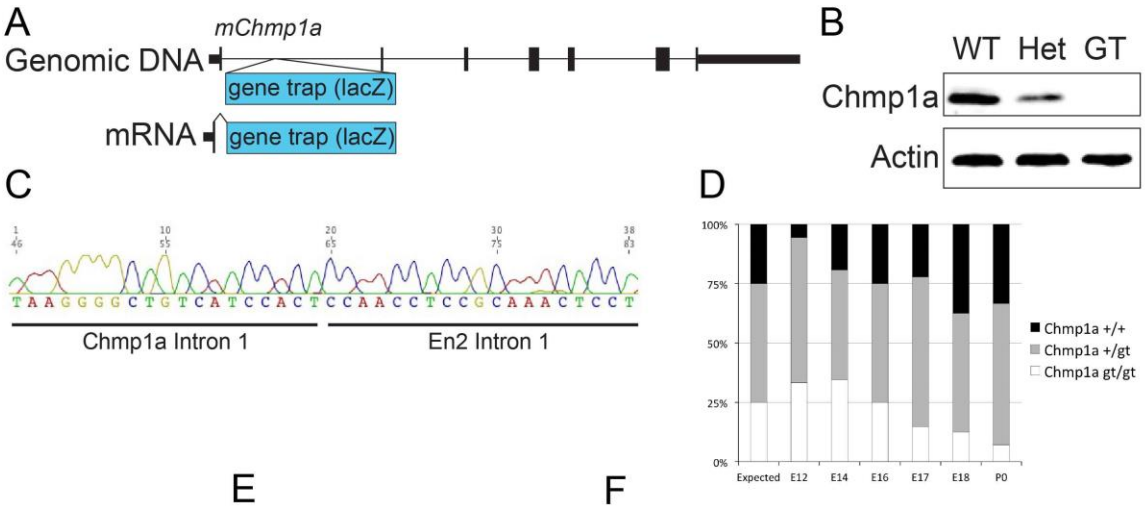

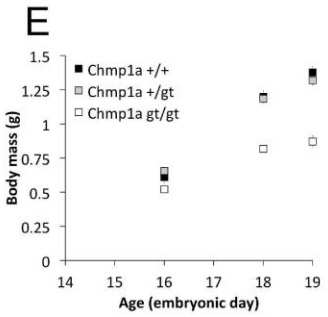

	E16	E18	P0
Chmp1a +/+	0.61	1.20	1.38
Chmp1a +/-	0.66	1.19	1.32
p-value	0.13	0.87	0.30

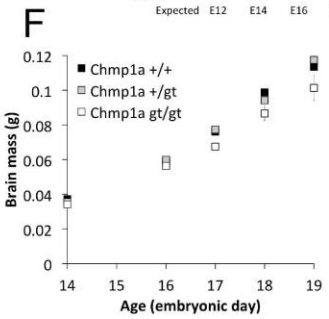

	E14	E16	E17	E18	P0
Chmp1a +/+	0.037	0.059	0.076	0.099	0.114
Chmp1a +/-	0.036	0.060	0.077	0.094	0.118
p-value	-	0.54	0.57	0.87	0.42

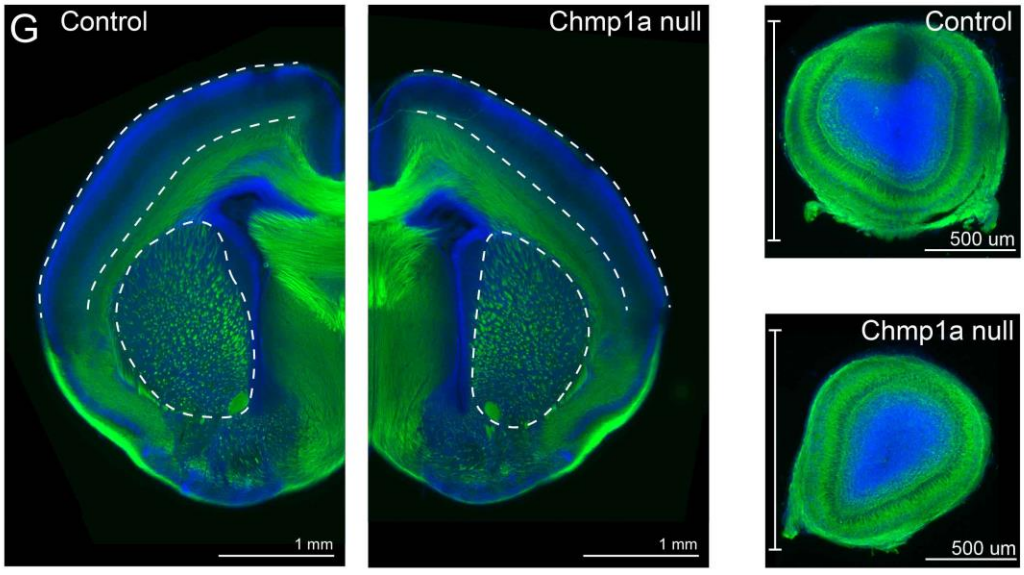

Supplemental Figure 1: *Chmp1a* gene trap mouse model

(A) Model of gene trap cassette in mouse *Chmp1a* locus. (B) Western blot shows *Chmp1a* null mice express no Chmp1a protein. (C) Sanger sequencing of genomic DNA in *Chmp1a* null mice shows fusion of *Chmp1a* intron 1 to *En2* intron 1 in GT cassette. (D) Mendelian ratios of *Chmp1a* GT litters during embryonic development. Expected Mendelian ratio is shown in the left bar. At late embryogenesis, *Chmp1a* gt/gt begin to die and few are recovered at P0. (E) *Chmp1a* +/gt embryos do not have a defect in embryonic development compared to *Chmp1a* +/+ embryos. Mass and p-values of +/+ vs +/gt are shown below, two-tailed t-test. (F) *Chmp1a* +/gt embryos do not have a defect in embryonic brain development compared to *Chmp1a* +/+ embryos. Mass and p-values of +/+ vs +/gt are shown below, two-tailed t-test. (G) *Chmp1a* null mouse telencephalon and olfactory bulb are hypomorphic.

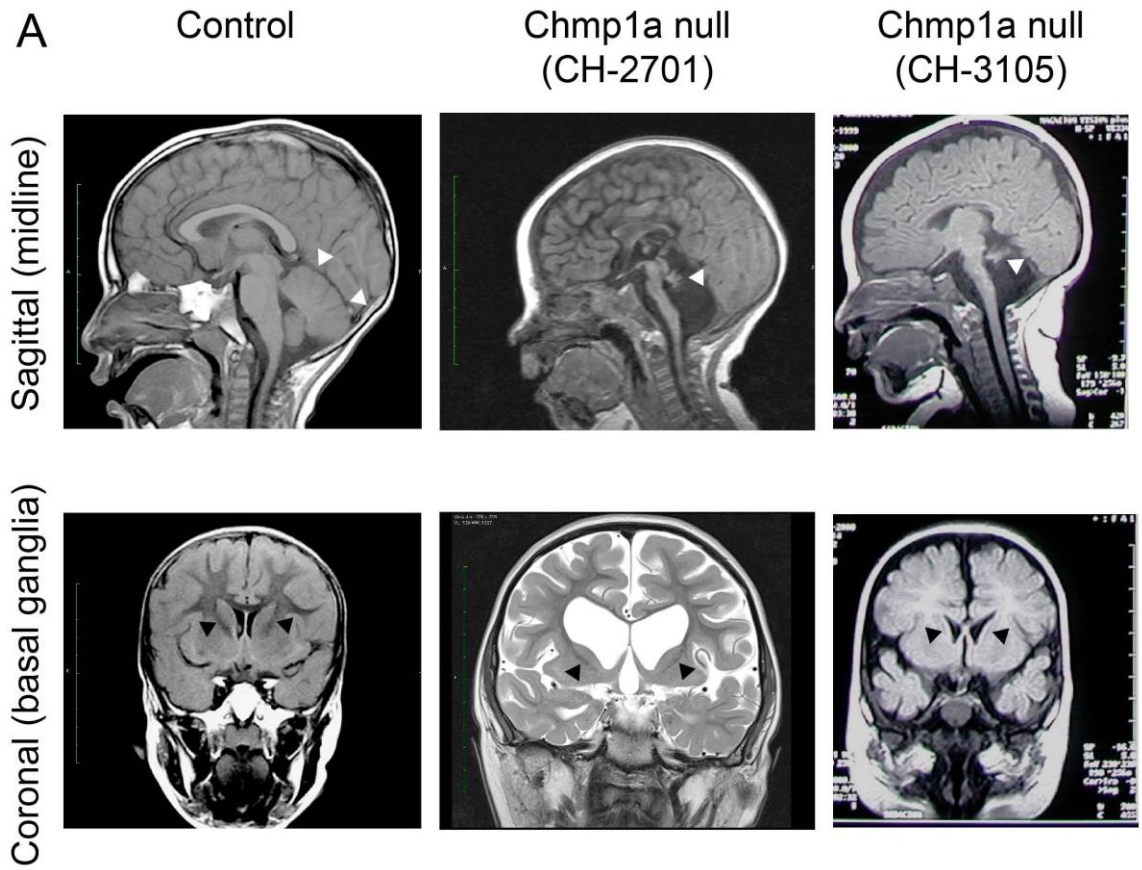

Supplemental Figure 2: MRI imaging of patients with *CHMP1A* null mutations

(A) MRI images of one control and two patients with *CHMP1A* null mutations. Control is a neurologically normal 2 year old male, CH-2701 is 6 month old female with Q30X *CHMP1A* mutation, and CH-3105 is 3 month old male with c.28-13G>A V33fs *CHMP1A* mutation (Mochida et al., 2012). Sagittal images show decreased head circumference (microcephaly) and severe cerebellar hypoplasia (arrowhead) in absence of CHMP1A. Coronal images show hypoplasia of caudate (arrowheads) in absence of CHMP1A.

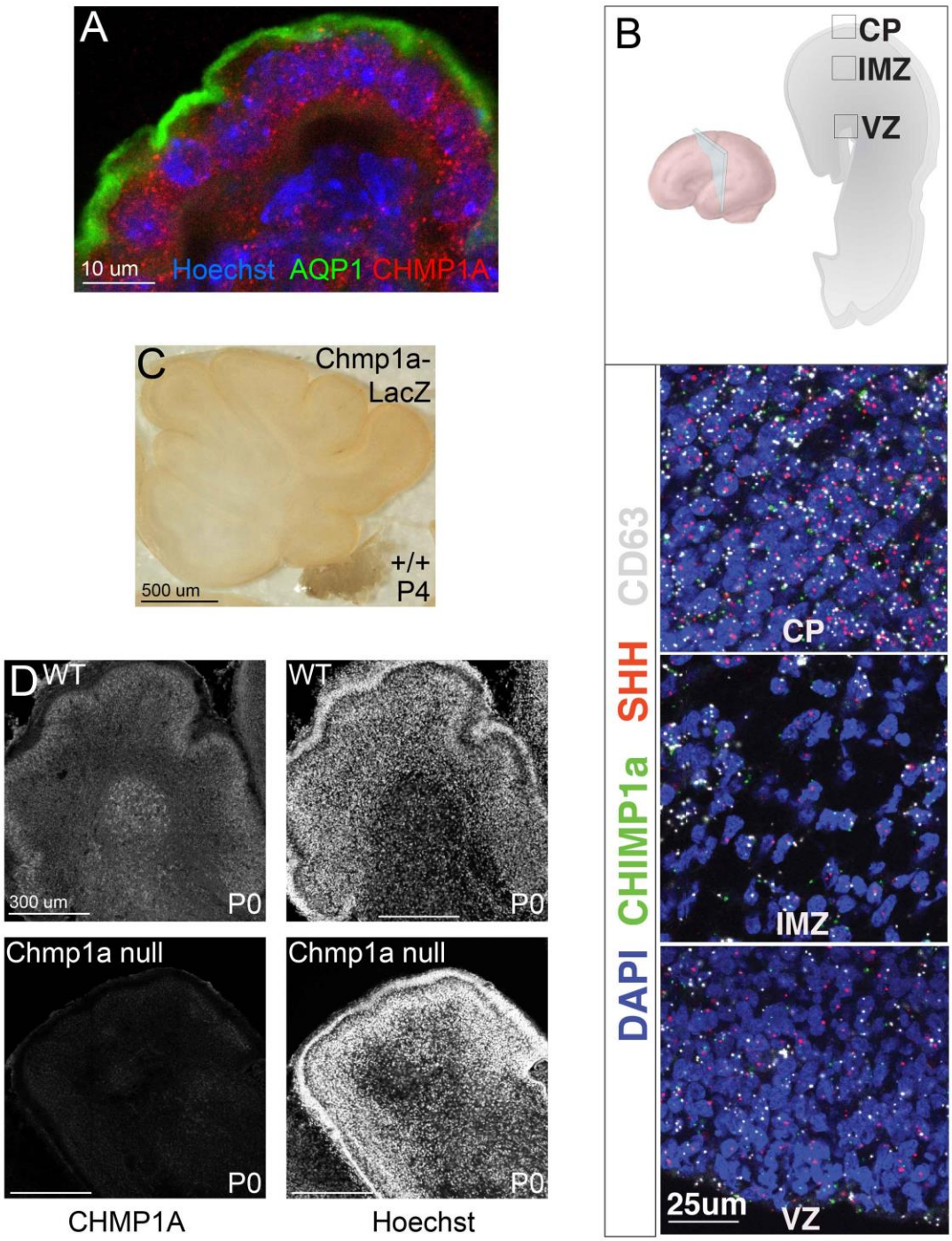

Supplemental Figure 3: *CHMP1A* RNAscope, ChP expression, and expression controls

(A) Chmp1a immunoreactivity is punctate in epithelial cells of hindbrain choroid plexus at P0. AQP1 labels ventricular surface. (B) *CHMP1A*, *SHH*, and *CD63* expression in developing human cortex by RNAscope. (C) Beta-gal staining in wild type mouse shows no signal in cerebellum or choroid plexus at P4. (D) Immunostain for Chmp1a shows no signal in *Chmp1a* null cerebellum at P0. All panels are representative image of ≥2 experiments.

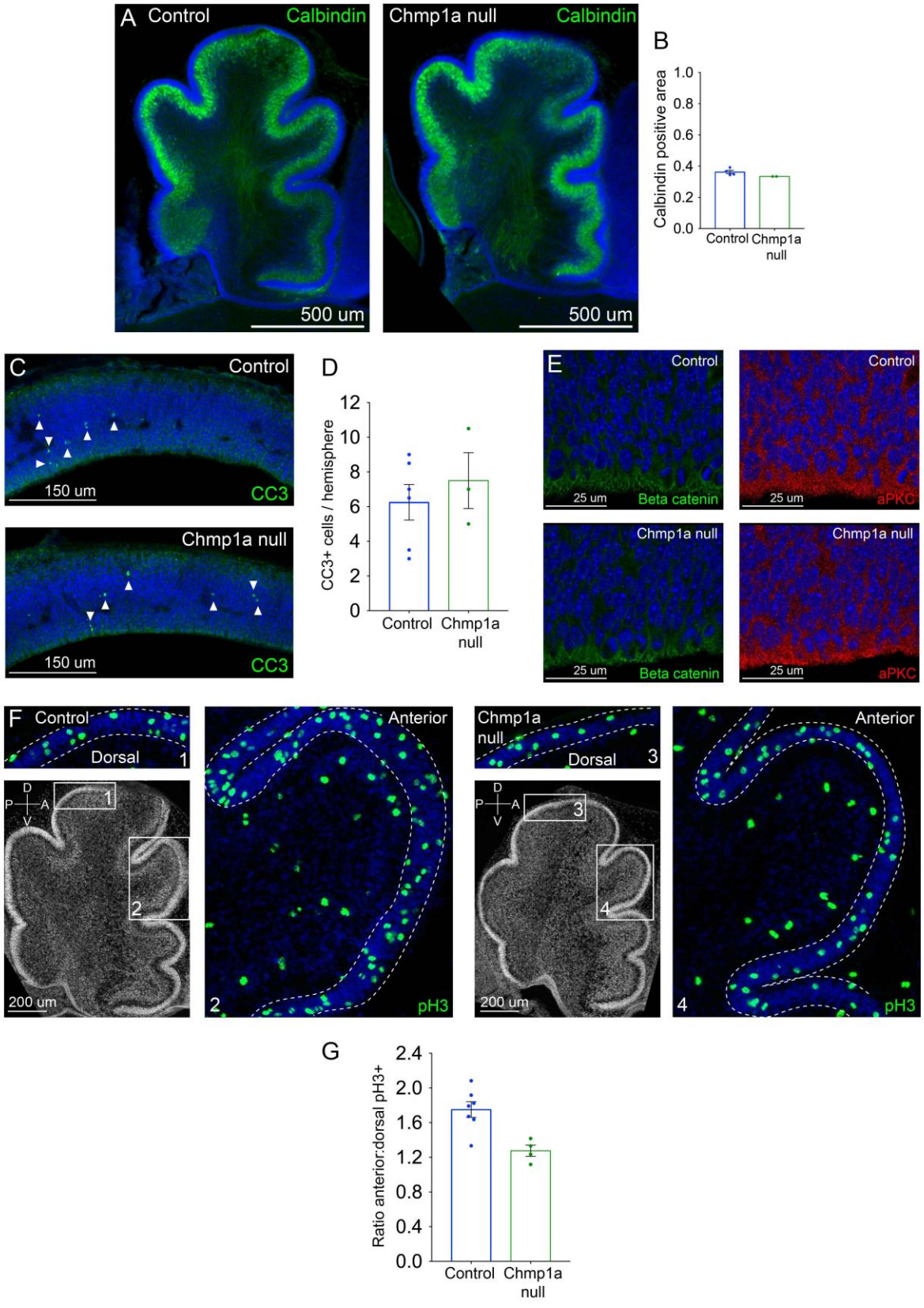
A Control
Calbindin
500 um
Chmp1a null
Calbindin
500 um
B
Calbindin positive area
1.0
0.8
0.6
0.4
0.2
0.0
Control
Chmp1a null
C
Control
150 um
CC3
Chmp1a null
150 um
CC3
D
CC3+ cells / hemisphere
12
10
8
6
4
2
0
Control
Chmp1a null
E
Control
25 um
Beta catenin
Control
25 um
aPKC
Chmp1a null
25 um
Beta catenin
Chmp1a null
25 um
aPKC
F
Control
Dorsal
1
D
P
A
V
1
2
200 um
Anterior
2
pH3
Chmp1a null
Dorsal
3
D
P
A
V
3
4
200 um
Anterior
4
pH3
G
Ratio anterior:dorsal pH3+
2.4
2.0
1.6
1.2
0.8
0.4
0.0
Control
Chmp1a null

Supplemental Figure 4: Developing cortex and cerebellum in *Chmp1a* null mouse

(A) Purkinje cell layer is intact in *Chmp1*a null P0 pups and unchanged compared to littermate controls. Immunostain for Calbindin labels Purkinje cells in control and *Chmp1a* null P0 cerebellum. (B) Fraction of cerebellum area covered by the Purkinje cell has no detectable difference in *Chmp1a* null pups compared to controls (Control: n=4, *Chmp1a* null: n=2, two-tailed t-test, $p = 0.16$). (C) During cortical development, there is no detectable increase in apoptosis in *Chmp1a* null embryos compared to controls. Apoptotic cells in developing cortex (E12.5) were labeled with immunostaining for cleaved caspase 3. (D) Quantification of (A), Control: n=6, *Chmp1a* null: n=3, two-tailed t-test, $p = 0.52$. (E) There is no detectable defect in cortical ventricular surface formation in *Chmp1a* null embryos. Immunostaining for beta-catenin and atypical protein kinase C, two proteins that localizes at the ventricular surface, showed no focal defects in ventricular surface or changes in protein distribution in *Chmp1a* null developing cortex (E14.5). Representative image of 2 experiments. (F) SHH drives GCP proliferation more in anterior lobe than in dorsal lobe. (G) Control littermates have 75% more mitotic GCPs in the anterior lobe compared to the dorsal lobe; in contrast, *Chmp1a* null pups have only 25% more mitotic GCPs in anterior lobe, Control: n=7, *Chmp1a* null: n=4, two-tailed t-test, $p = 0.005$. Two-tailed, unpaired t-test, * $p < 0.05$, ** $p < 0.01$.

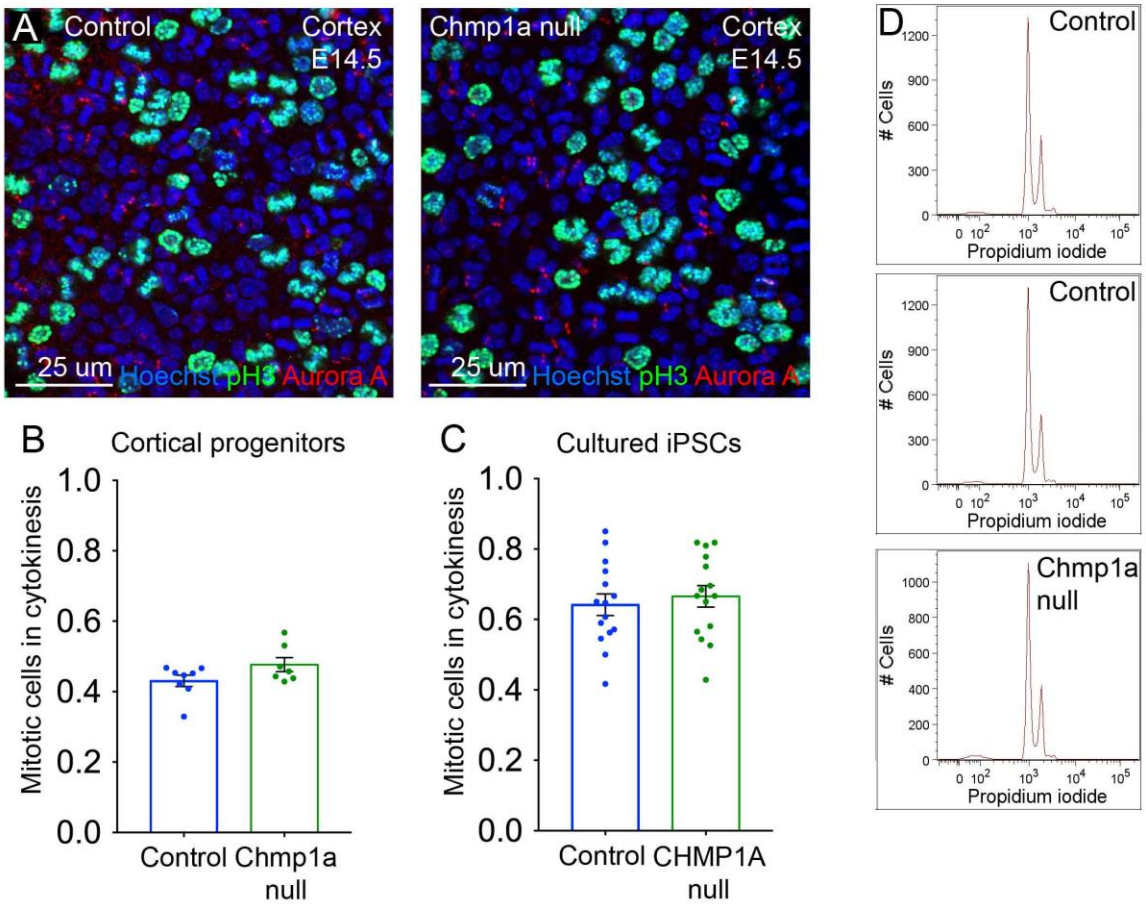

Supplemental Figure 5: *Chmp1a* is not required for cytokinesis

(A) Cytokinesis disruption was not detected in the absence of CHMP1A. Ventricular surface of mouse cortex and cultured iPSCs were immunostained for pH3 and aurora A (images show mouse cortex ventricular surface). pH3 labels early mitotic cells and aurora A labels the midbody of late mitotic cells. The fraction of mitotic cells in cytokinesis was calculated as: (Aurora A) / (Aurora A + pH3). (B) There was no detectable difference in the fraction of cells in cytokinesis in ventricular cortical progenitors of *Chmp1a* null embryos compared to littermate controls (Control: n=8, *Chmp1a* null: n=7, two-tailed t-test, p = 0.093). (C) There was no detectable difference in fraction of cells in cytokinesis in *CHMP1A* null and WT cultured iPSCs (Control: n=15, *Chmp1a* null: n=15, two-tailed t-test, p = 0.59). (D) Propidium iodide staining of *Chmp1a* null and control MEF lines. There was no detectable difference in distribution of DNA content between *Chmp1a* null (n=1) and control MEFs (n=2).

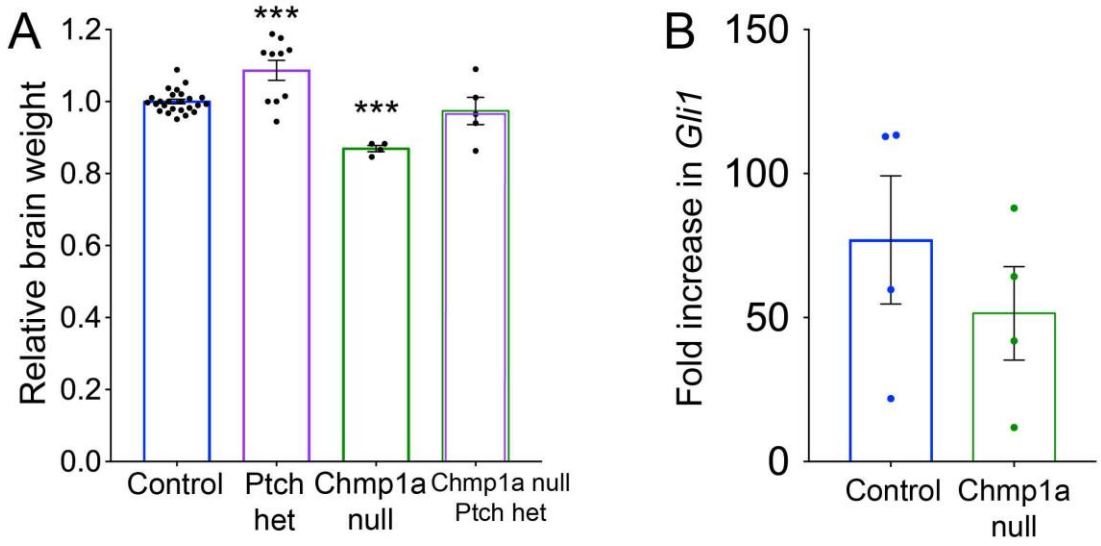

Supplemental Figure 6: *Chmp1a* null ; *Ptch* mutant mouse and *Gli1* in MEFs

(A) Brain weight of *Chmp1a* null ; *Ptch* heterozygous mouse embryos at E18.5/P0 (Control: n=25, *Ptch* het: n=10, *Chmp1a* null: n=4, Chmp1a null ; *Ptch* het: n=5, two-tailed t-test, *Ptch* het: $p < 0.001$, *Chmp1a* null: $p < 0.001$, *Chmp1a* null ; *Ptch* het: $p = 0.22$). (B) *Shh* signaling is intact in *Chmp1a* null MEFs. MEFs were stimulated with SAG and *Gli1* expression increase was used to measure *Shh* pathway activation. There is no detectable difference between *Chmp1a* null and littermate control MEFs (Control: n=4, *Chmp1a* null: n=4, two-tailed t-test, $p = 0.39$). Two-tailed, unpaired t-test, ** $p < 0.001$.

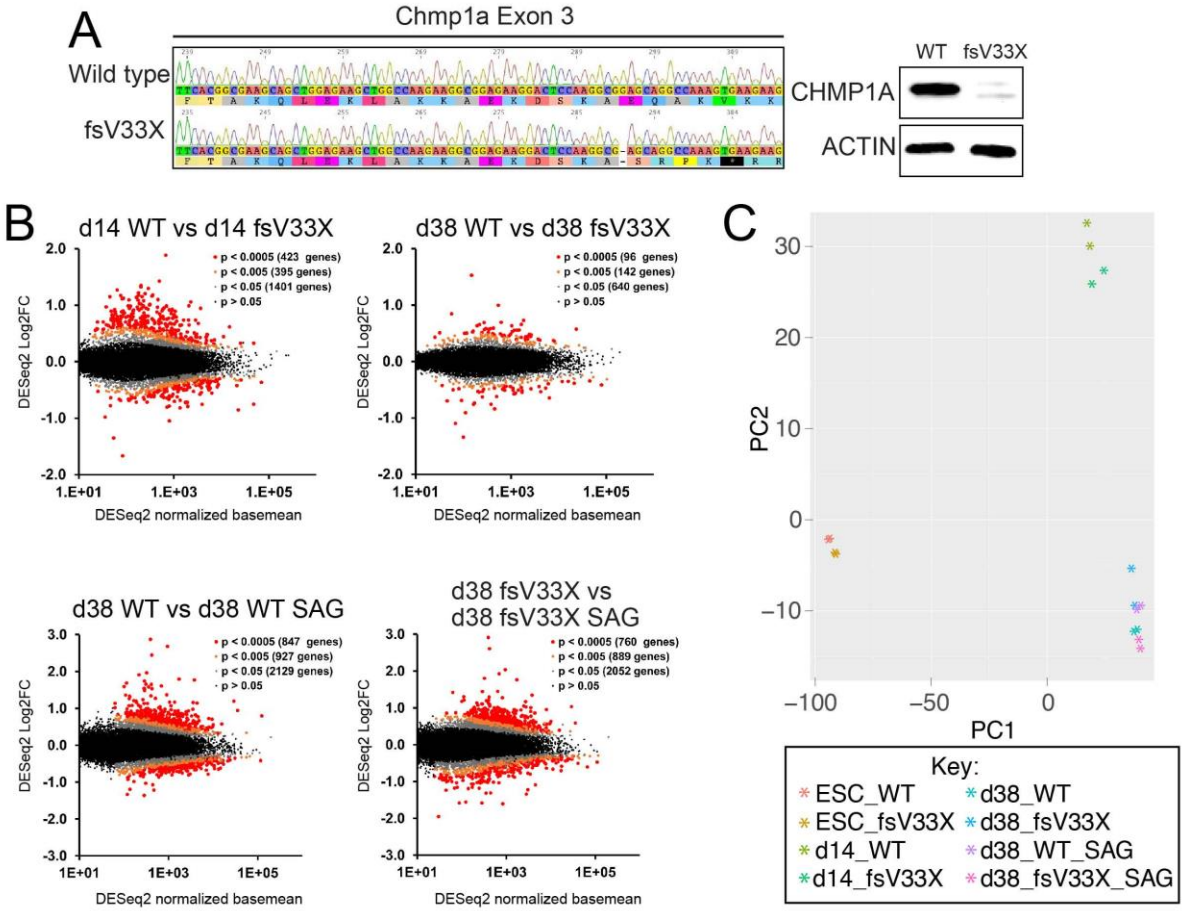

Supplemental Figure 7: Human organoid RNA sequencing quality control metrics

(A) Sanger sequencing showing wild type and 1 bp frameshift deletion and resulting premature STOP codon in *CHMP1A* null iPSC line (fsV33X). *CHMP1A* null iPSCs do not express CHMP1A protein. (B) MA plots of pairwise comparisons of organoid RNA-sequencing data. Data shows output values of DESeq2 analysis, Y-axis shows DESeq2 corrected Log2 fold-change, X-axis basemean expression levels. Colored dots represent genes according to their p-value. (C) PCA plot of all samples and replicates used in this study after normalization using DESeq2.

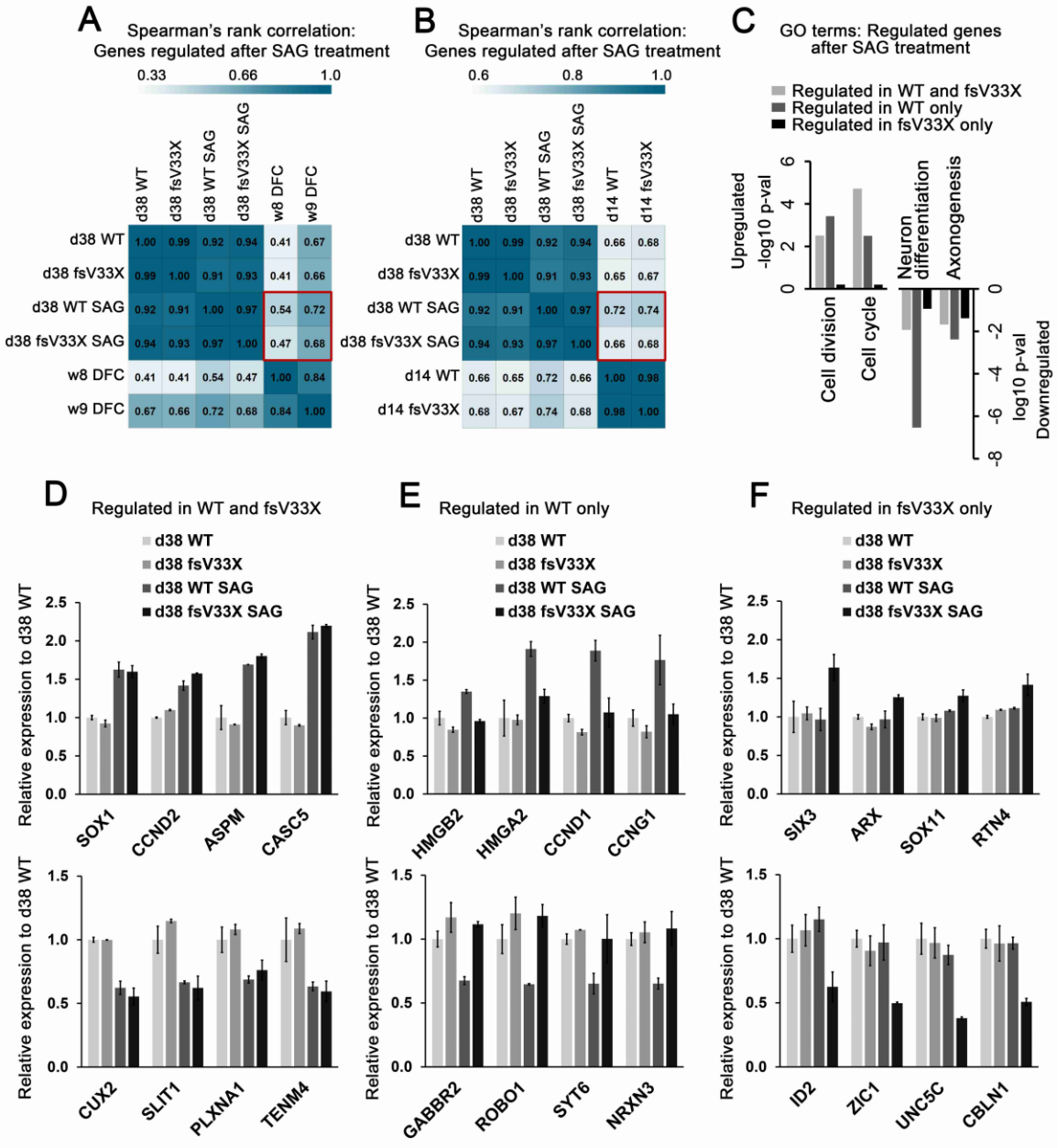
A
Spearman's rank correlation:
Genes regulated after SAG treatment
0.33
0.66
1.0
d38 WT
d38 fsV33X
d38 WT SAG
d38 fsV33X SAG
w8 DFC
w9 DFC
B
Spearman's rank correlation:
Genes regulated after SAG treatment
0.6
0.8
1.0
d38 WT
d38 fsV33X
d38 WT SAG
d38 fsV33X SAG
d14 WT
d14 fsV33X
C
GO terms: Regulated genes
after SAG treatment
Regulated in WT and fsV33X
Regulated in WT only
Regulated in fsV33X only
Upregulated
-log10 p-val
Cell division
Cell cycle
Neuron differentiation
Axonogenesis
log10 p-val
Downregulated
D
Regulated in WT and fsV33X
E
Regulated in WT only
F
Regulated in fsV33X only
Relative expression to d38 WT
SOX1
CCND2
ASPM
CASC5
CUX2
SLIT1
PLXNA1
TENM4
HMGB2
HMGA2
CCND1
CCNG1
GABBR2
ROBO1
SYT6
NRXN3
SIX3
ARX
SOX11
RTN4
ID2
ZIC1
UNC5C
CBLN1

Supplemental Figure 8: Gene expression changes following SAG treatment of human organoids

(A) Comparison of d38 organoid data to Brainspan data using Spearman's rank correlation. Highlighted in red shows SAG treatment of control organoids increases correlation with w9 and more strongly with w8 DFC data compared to DMSO treated control organoids. *CHMP1A* null organoids respond as well but to a lesser extent. (B) Comparison of d38 organoid data to d14 organoid data. Similarly to panel A, SAG treated control organoids show better correlation with early stage day14 organoids. (C) GO analysis of differentially expressed genes. SAG treatment leads to upregulation of proliferation genes and downregulation of differentiation genes in both control and *CHMP1A null* cerebral organoids (light grey bars). There are also genes regulated only in control or only in *CHMP1A* null organoids, which were analyzed as separate groups (dark grey bars, black bars respectively). Control organoids show extra sets of genes positively regulating cell cycle, and negatively regulating differentiation. (D), (E), (F) Representative genes and their expression changes from analyses and groups shown in panels A, B and C.

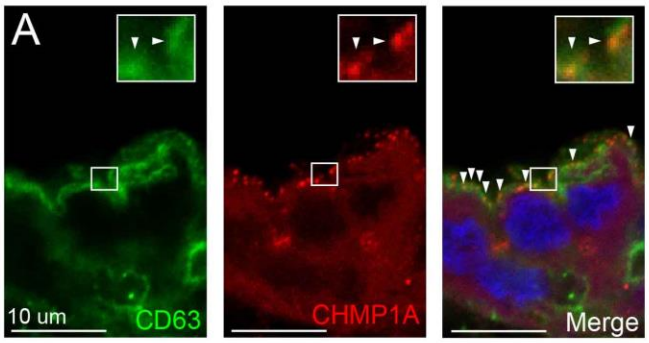
A
10 um
CD63
CHMP1A
Merge

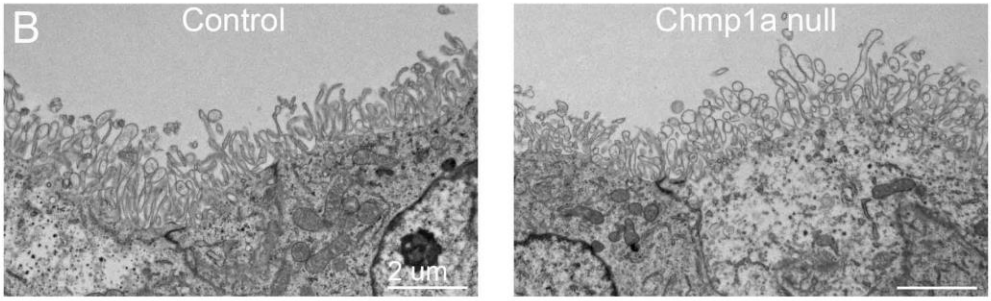
B
Control
2 um
Chmp1a null

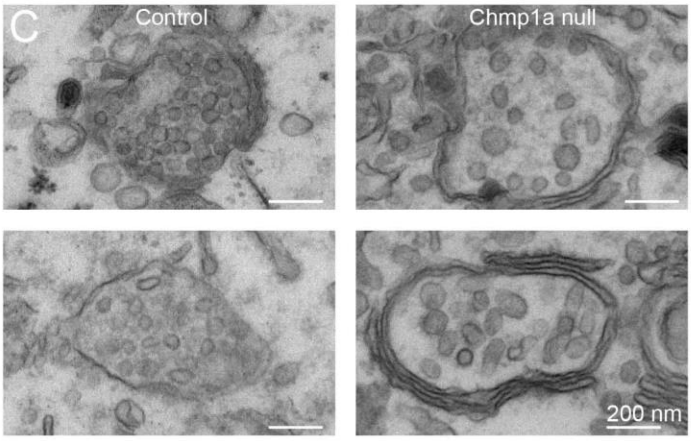
C
Control
Chmp1a null
200 nm

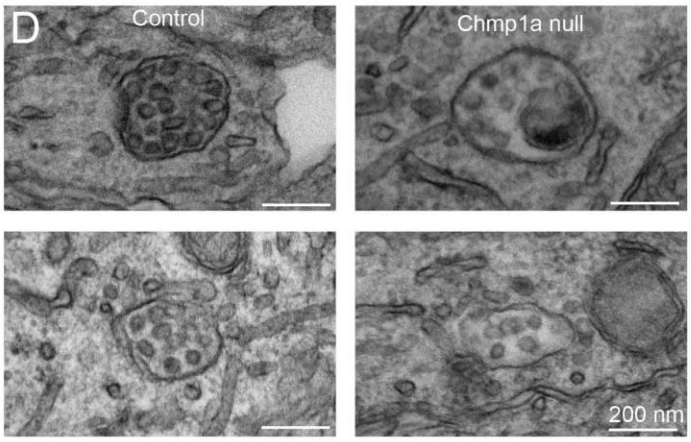
D
Control
Chmp1a null
200 nm

Supplemental Figure 9: Choroid plexus epithelial surface and additional MVBs

(A) Partial colocalization of CHMP1A and CD63 puncta (inset and arrowheads) at the ventricular surface of human hindbrain ChP (11 d.o.). Representative image of 2 experiments. (B) There is no detectable defect in choroid plexus epithelial cell microvilli in *Chmp1a* null embryos at E17.5. (C) Additional examples of choroid plexus epithelial cell MVBs in control and *Chmp1a* null littermates. *Chmp1a* null MVBs contain fewer ILVs and often contain large ILVs. (D) Additional examples of Purkinje cell MVBs from *Chmp1a* null P0 pups and littermate controls. *Chmp1a* null MVBs contain fewer ILVs than controls.

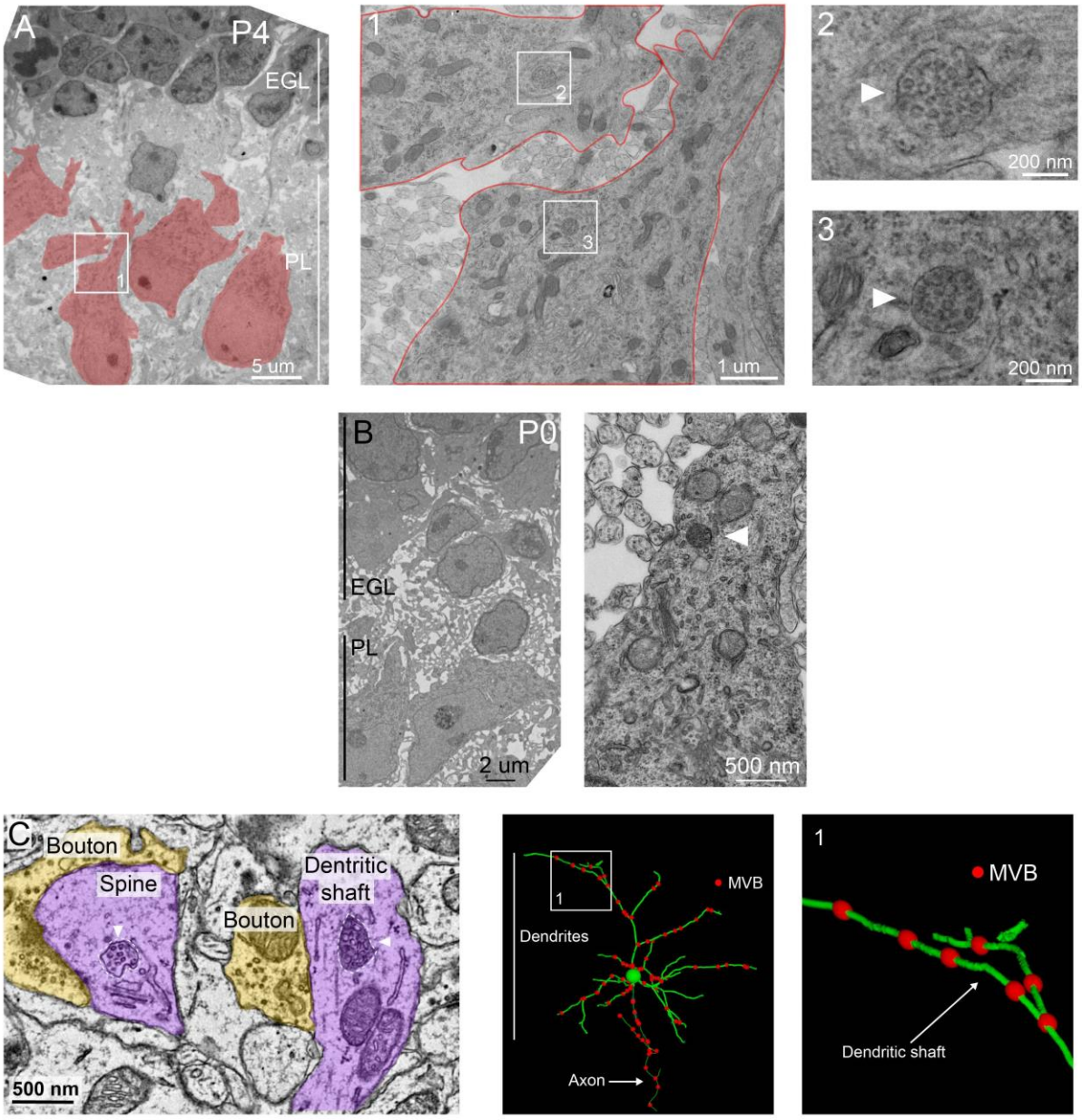

Supplemental Figure 10: MVBs localize to dendrites in postmitotic neurons

(A) MVBs are in distal (2) and proximal (3) Purkinje cell dendrites in developing cerebellum at P4. (B) MVBs are located in Purkinje cell dendrites at P0. (C) MVBs in dendrites of layer II/III cortical pyramidal neurons. High magnification image shows a MVB (white arrowhead) near an excitatory synapse in a pyramidal cell dendritic spine and near an inhibitory synapse in a dendritic shaft. MVBs locations are represented by red dots in a rendered 3D TEM reconstruction of a serially sectioned pyramidal neuron.

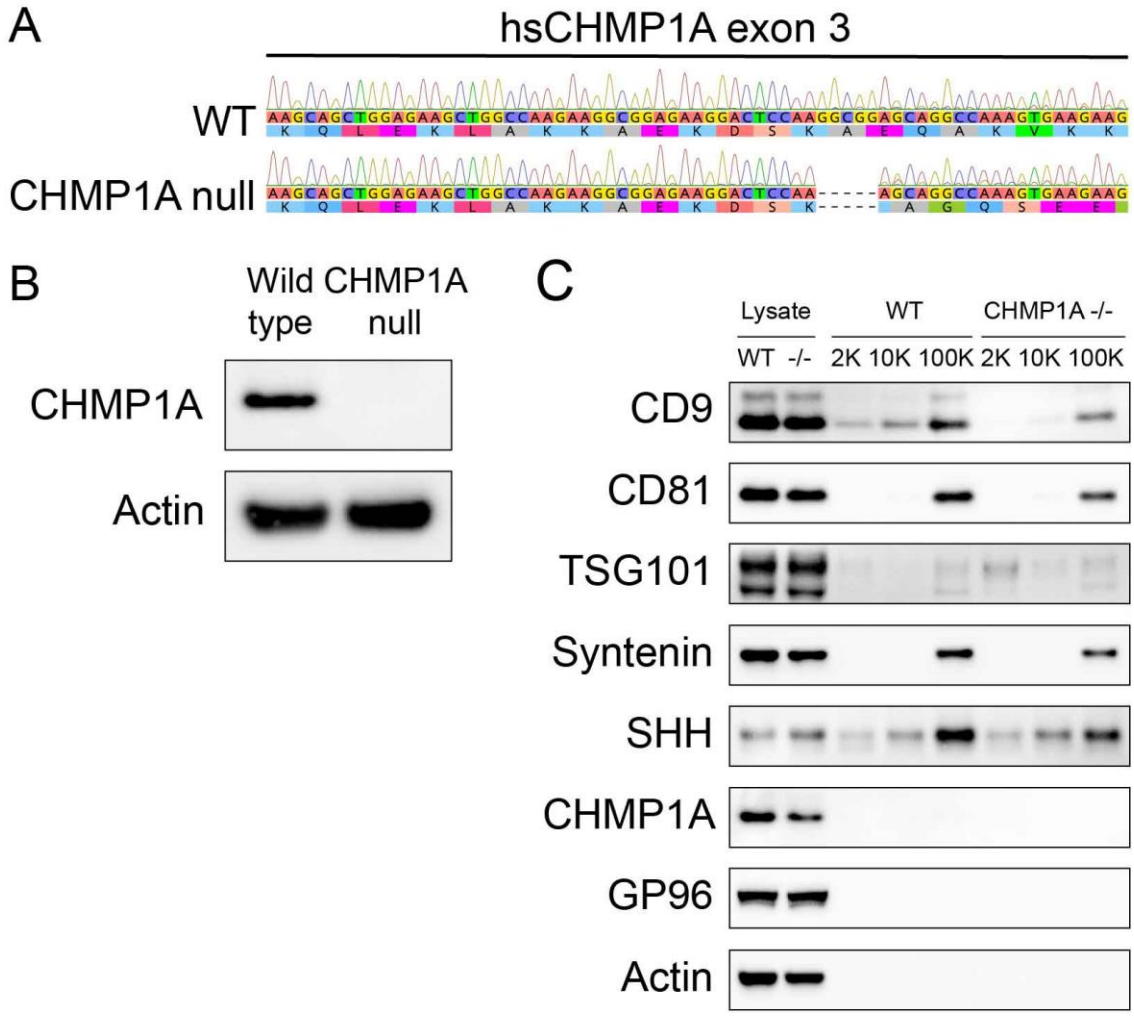

Supplemental Figure 11: *CHMP1A* null SVG-A cell lines

(A) *CHMP1A* null SVG-A cell line Sanger sequencing shows a 5 bp frameshift deletion in exon 3. This mutation creates a stop codon after exon 3. (B) No CHMP1A protein is detected by immunoblot in *CHMP1A* null SVG-A cells. (C) 100K EV fraction purified from pooled SVG-A cells transfected with *CHMP1A* null gRNA and Cas9. As we found in a stable monoclonal CHMP1A null SGV-A line, secretion of exosomal markers and SHH is decreased.

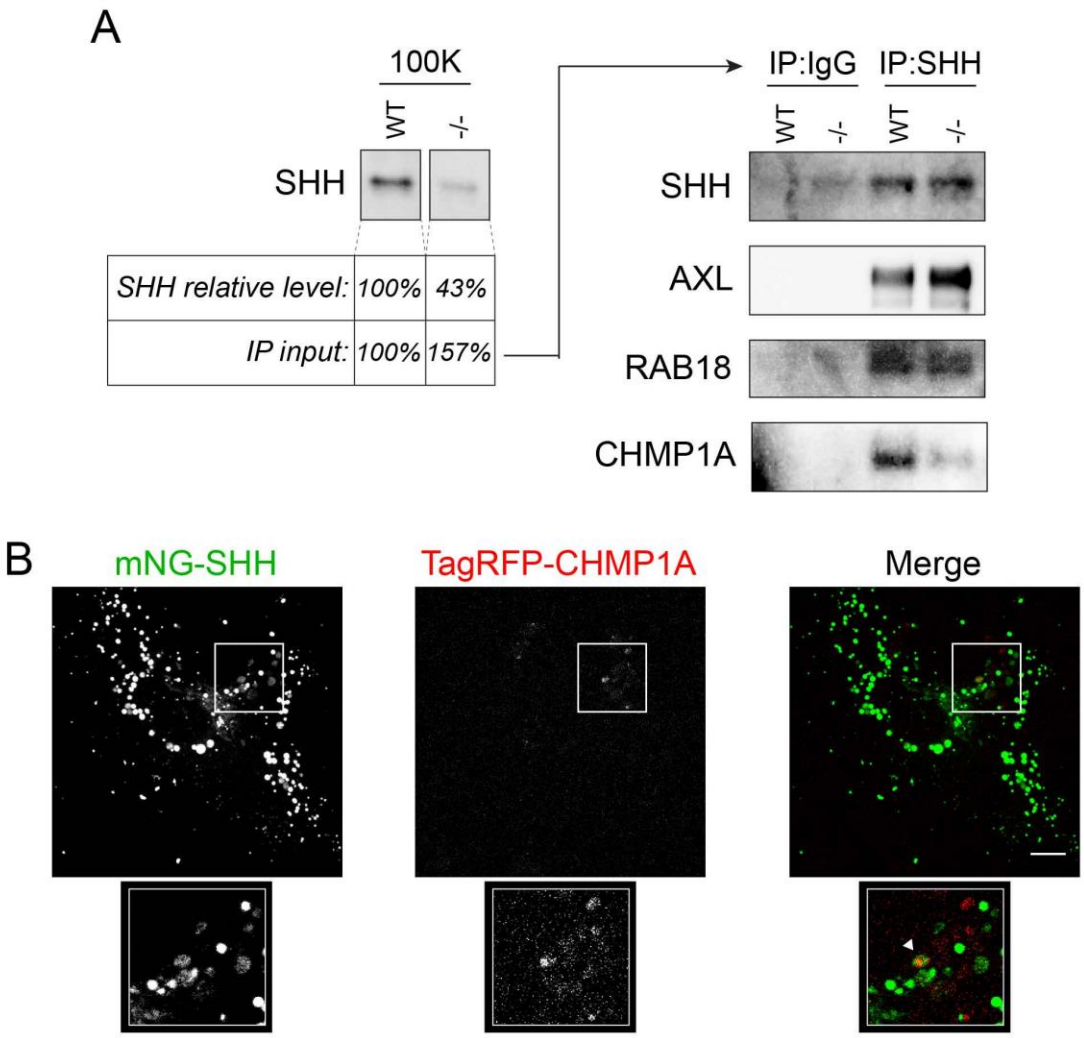

Supplemental Figure 12: CHMP1A is associated with ART-EV complexes and partially co-distributes with intracellular SHH

(A) SHH-positive vesicles from the 100K pellet of WT and *CHMP1A* null SVGA cells were immunoisolated (right panel) using different input amounts (left panel), so that the SHH levels in the WT and KO input fractions are equivalent. WB analysis of the bound material shows CHMP1A in SHH-EVs from WT but not KO cells, while RAB18 and AXL are present in both fractions. (B) SVG-A cells were transfected with TagRFP-CHMP1A and mNG-SHH expressing plasmids and 48 h later, 15 z stacks of 0.5 µm were acquired every 5 seconds on a spinning disk confocal microscope using 488 and 561 nm lasers lines and associated filter sets. Snapshots show a z projection for each channel and the color-coded merge (upper panels). Cropped images (lower panels) show a single z plane, and the arrowhead points at colocalizing CHMP1A and SHH signals. Scale bar is 10 µm. See full video in Supplemental Movie 1.